THE ASTROPHYSICAL JOURNAL, 461:933–950, 1996 April 20


# THE STRUCTURE OF THE BOUNDARY LAYER IN PROTOSTELLAR DISKS[1]

W. KLEY
MPG AG-Gravitation, Friedrich-Schiller-Universität, Max-Wien-Platz 1, D-07743 Jena, Germany; wak@gravi.physik.uni-jena.de
AND
D. N. C. LIN
Lick Observatory, University of California, Santa Cruz, CA 95064; lin@lick.ucsc.edu
*Received 1995 June 20; accepted 1995 October 17*

## ABSTRACT

Circumstellar disks are commonly associated with pre–main-sequence stars. Under the action of viscous stress, angular momentum is transferred outward and matter diffuses inward. With the aid of a fully two-dimensional, axisymmetric hydrodynamical scheme we investigate the accretion of matter from protostellar disks onto their central stars. In order to obtain an asymptotic steady state solution we follow the evolution of the flow for over $10^3$ dynamical timescales. For typical ranges of accretion rates we confirm the existence of two quasi-equilibrium states of the disk, separated by thermal instability. For relatively low accretion rates ($<10^{-6}\ M_\odot\ \mathrm{yr}^{-1}$), typical for classical T Tauri stars, the disk is geometrically thin and fully convective. In the region adjacent to the stellar surface, i.e., in the boundary layer, the disk is optically thin. For relatively high accretion rates (more than a few $10^{-5}\ M_\odot\ \mathrm{yr}^{-1}$), typical for FU Orionis systems, the disk is geometrically thick and radiative. The incoming matter spreads rapidly around the protostellar envelope to form a dense, hot shell. Within the stellar envelope, and in the disk for a low mass-inflow rate, we were able to resolve directly several convection cells, which are driven by the ionization of hydrogen. These eddies provide an effective viscous stress such that the accretion of rapidly rotating disk material generally induces an increase in the spin of the outer convective envelope of the star.

*Subject headings:* circumstellar matter — hydrodynamics — stars: formation — stars: pre–main-sequence

## 1. INTRODUCTION

Around many young stellar objects, the excess infrared spectrum resembles that expected from viscously evolving protostellar disks (Adams, Lada, & Shu 1988; Sargent & Beckwith 1987; Sargent et al. 1988; Beckwith 1994). At the disk's inner edge, gas leaves the disk and joins the central, accreting star. If the accreting star is magnetized with a field strength in excess of $10^3$ G, the interface may be regulated by a magnetosphere (Königl 1991; Shu et al. 1994). In the weak-field (or high mass flux) limit, however, the disk may make direct contact with the surface layer of the protostar (Popham et al. 1993). In this paper, we consider the protostar-disk interaction of the latter, nonmagnetic, configuration.

The observed stellar rotation rate is generally much slower than the breakup velocity (Cohen & Kuhi 1979). In order for the accreted matter to leave the disk and join the star, it must decelerate in a narrow transition region, usually referred to as the boundary layer (BL). This terminology in the astrophysical context differs slightly from that used in standard fluid dynamics. Within the BL of a star (with mass $M_*$ and radius $R_*$), the fluid elements' angular velocity decreases from their Keplerian value, $\Omega_K = (GM_*/R_*^3)^{1/2}$, to the much smaller stellar rotation rate $\Omega_*$. The enormous strain induced by the large velocity gradient near the stellar surface may lead to shearing instabilities and induce turbulence. Turbulent motion may also be generated from convective, MHD, or other instabilities (Pringle 1981; Balbus & Hawley 1991). The effective Reynolds stress leads to frictional interaction of the stellar surface layer with the inner disk. The luminosity of the BL can be calculated from the energy and angular momentum conservation laws, taking the acceleration of the star (i.e., the transfer of energy and momentum into the star) into account (see, e.g., Shakura & Sunyaev 1973; Lynden-Bell & Pringle 1974; Papaloizou & Stanley 1986). For a radially thin BL, one obtains

$$L_{\mathrm{BL}} = \frac{1}{2} L_{\mathrm{acc}} \left[ 1 - \frac{\Omega_*}{\Omega_K(R_*)} \right]^2 , \qquad (1)$$

where $L_{\mathrm{acc}} = GM_* \dot{M}/R_*$ is the rate at which gravitational energy is released if matter falls at an accretion rate $\dot{M}$ from infinity to $R_*$. Thus, the amount of dissipated energy released in the BL is substantial and can equal the total accretion energy of the outer protostellar disk. The combination of a small emitting area with a high energy output leads to a strong contribution of the BL radiation in the shorter wavelengths.

This BL emission has been observed in several classical T Tauri stars (Bertout, Basri, & Bouvier 1988). It is usually characterized by strong emission lines, UV excess, and optical veiling (Basri & Bertout 1993), which are indicative that this region is relatively hot ($>7000$ K) and optically thin. Model analysis indicates that $\dot{M} \sim 10^{-7}\ M_\odot\ \mathrm{yr}^{-1}$ in these systems (Basri & Bertout 1989). Evidence for disks is also found in another class of young stellar objects, FU Orionis stars, in which $\dot{M} > 10^{-5}\ M_\odot\ \mathrm{yr}^{-1}$ (Hartmann, Kenyon, & Hartigan 1993). However, there is little or no evidence of BL emission in FU Orionis systems. An important task is determination of the cause of this basic difference between these two limiting cases.

The only theoretical analyses of the BL structure in protostellar accretion disks have been carried out with a one-dimensional thin-disk approximation (Bertout & Regev

[1] Lick Observatory Bulletin.

1992; Popham et al. 1993) in the steady state limit. In this approach, the disk *and* the boundary layer are assumed to be axisymmetric and flat. The structure equations are averaged in the direction normal to the disk plane ($z$) and depend solely on the distance from the origin ($r$). The radial distribution of physical quantities such as the surface density $\Sigma$, temperature $T$, and velocities are expressed in terms of their midplane values. This approximation may be adequate in most regions of the disk, where the condition for local energy equilibrium is satisfied, i.e., the energy dissipated at a given radius is radiated locally. However, such a prescription may no longer be valid in the BL region, where large radial gradients of all physical quantities lead to efficient radial transport of both momentum and energy. Although some attempts have been made to include the contribution of radial diffusion (Narayan & Popham 1993), these treatments are still based on the vertical-averaging approximation. However, the radiative and advective flux of energy and momentum may be rapidly varying functions of both $r$ and $z$.

In addition, in the contact region on the stellar surface, in order for the newly acquired disk material to be accreted, it may spread over the entire stellar surface, and the main flow may be primarily in the vertical direction (Shu et al. 1993). Also, in both the envelope of a rotating star and a moderately thick accretion disk, local thermodynamic and hydrostatic equilibrium cannot be satisfied simultaneously, and meridional circulation may play an important role in both momentum and energy transfer (Kippenhahn & Thomas 1982; Kley, Papaloizou, & Lin 1993a). Finally, these regions may be subject to thermal instability that would make steady state solutions physically unattainable (Bell & Lin 1994). Such an instability may be responsible for unsteady flows in protostellar disks, such as FU Orionis outbursts (Hartmann & Kenyon 1985; Lin & Papaloizou 1985). All of these considerations indicate that the investigation of the evolution of the disk/star boundary layer requires a multidimensional approach.

Numerical computation is a fruitful and effective method for resolving complex multidimensional flow patterns. In principle, the structure and stability of the BL region should be analyzed with a general three-dimensional treatise. However, the hardware requirements for a fully three-dimensional, time-dependent solution are beyond the current availability of computational resources. For computational convenience, we simplify the analysis to the two-dimensional limit with an idealized axisymmetric approximation. With this method we are able to resolve the vertical structure throughout the entire disk and examine the flow pattern as gas leaves the disk and joins onto the protostellar surface. By utilizing this time-dependent scheme, it is also possible to examine the thermal stability and long-term evolution of the disk. However, our approximation does not permit the study of any nonaxisymmetric shearing instability.

Our basic approach is based on the methods used successfully in studying the two-dimensional BL structure in cataclysmic variable stars (Kley 1989, 1991). In those calculations it was possible to follow the evolution over only a few dynamical timescales. We have modified and improved the numerical method and are now able to evolve a system for over $10^3$ dynamical timescales, a considerable improvement. In § 2 we present the basic equations and underlying physics and describe briefly the numerical method of solution. In § 3 we describe the formulation of the model setup. The analysis of a standard model is presented in § 4. We describe the dependence of the structure and evolution of BL flow on the mass-influx rate and viscosity in § 5. Finally, in § 6 we discuss the implication of our results.

## 2. EQUATIONS

In order to study the flow pattern near the stellar surface, we find it convenient to use spherical polar coordinates $(R, \varphi, \zeta)$, where $R$ is the radial distance, $\varphi$ is the azimuthal angle, and $\zeta = \pi/2 - \theta$ is the polar angle measured from the equatorial plane. (We will denote the cylindrical radius with a lowercase $r$.) In this coordinate system the partial differential equations for the gas density, three velocity components, and gas energy read

$$\frac{\partial \rho}{\partial t} + \nabla \cdot (\rho \boldsymbol{u}) = 0 , \tag{2}$$

$$\frac{\partial(\rho u_R)}{\partial t} + \nabla \cdot (\rho u_R \boldsymbol{u}) = \rho R\left(\frac{u_\zeta^2}{R^2} + \Omega^2 \cos^2 \zeta\right) - \frac{\partial p}{\partial R} - \rho \nabla \Psi + \nabla \cdot \boldsymbol{t}_R + \frac{1}{R} t_{RR} , \tag{3}$$

$$\frac{\partial(\rho u_\zeta R)}{\partial t} + \nabla \cdot (\rho u_\zeta R \boldsymbol{u}) = -\rho R^2 \Omega^2 \cos \zeta \sin \zeta - \frac{\partial p}{\partial \zeta} + \nabla \cdot (R \boldsymbol{t}_\zeta) + (\tan \zeta) t_{\varphi\varphi} , \tag{4}$$

$$\frac{\partial(\rho h)}{\partial t} + \nabla \cdot (\rho h \boldsymbol{u}) = \nabla \cdot (R \cos \zeta) \boldsymbol{t}_\varphi , \tag{5}$$

$$c_v \rho\left[\frac{\partial T}{\partial t} + (\boldsymbol{u} \cdot \nabla) T\right] = -p \nabla \cdot \boldsymbol{u} + \Phi - \nabla \cdot \boldsymbol{F} . \tag{6}$$

Here we use the following notation: $\rho$ denotes density; $\boldsymbol{u} = (u_R, u_\varphi, u_\zeta)$, velocity components; $\Omega = u_\varphi/(R \cos \zeta)$, angular velocity; $h = \Omega R^2 \cos^2 \zeta$, specific angular momentum; $T$, temperature; $p$, gas pressure; $c_v$, specific heat; and $\Psi = GM_*/R$, the static gravitational potential of the accreting star with mass $M_*$. The equations include explicitly all components of the viscous stress tensor $\mathbf{T}$ in the momentum and energy equation (Kley 1989), which has the vector components $(\boldsymbol{t}_R, \boldsymbol{t}_\varphi, \boldsymbol{t}_\zeta)$, where $\boldsymbol{t}_i = (t_{iR}, t_{i\varphi}, t_{i\zeta})$, $i = (R, \varphi, \zeta)$. The explicit forms of the components can be found in textbooks (e.g., Tassoul 1978). In the energy equation, $\Phi = (2\eta)^{-1} \mathrm{Tr}\,(\mathbf{T}^2)$ is the viscous dissipation, where $\eta$ is the dynamical viscosity coefficient, and $\boldsymbol{F}$ is the radiative energy flux.

In our previous two-dimensional analysis of the BL in cataclysmic variable stars (Kley 1991), we separated gas and radiation temperatures. Such a treatment is necessary for investigating the thermal structure and radiative properties of both the opaque and optically thin regions of the disk. However, that approach is computationally intense enough that we have not been able to examine the evolution of the disk for more than a few dynamical timescales. Those results indicate that significant difference between the gas and radiation temperatures occurs only in the tenuous optically thin regions, which do not have any significant impact on the dynamical structure and evolution of the disk.

In the present context, we are interested in the asymptotic equilibrium solutions, which are only attainable after many dynamical timescales. Therefore, we adopt here a modified

algorithm. To follow the dynamical evolution of the disk, we assume local thermodynamic equilibrium so that the contribution of radiation to the total energy density is negligibly small and the radiation transport may be incorporated directly into the thermal energy equation. In this approximation, the radiative-flux vector is given by

$$\boldsymbol{F} = -\frac{\lambda 4aT^3}{\rho(\kappa+\sigma)}\nabla T\,, \tag{7}$$

where $\kappa$ is the Rosseland mean opacity, $\sigma$ the scattering coefficient, $a$ the radiation constant, and $\lambda$ the flux limiter. This procedure greatly simplifies the numerical solution of equations (2)–(6) and leads to a considerable reduction of the required CPU time. With this improvement, it is possible to follow the evolution of the system on a viscous timescale. However, this "one-fluid" approximation is inadequate for the investigation of optically thin regions of the disk, such as the "corona," where radiation contributes a substantial fraction of the total energy density. In order to determine the thermal structure and the radiative properties in both the opaque and optically thick regions at some specific epochs of disk evolution, a more general "two-temperature" numerical method would have to be applied.

The gas is assumed to be a pure mixture of hydrogen and helium with mass fractions $Z_{\rm H} = 0.7$, $Z_{\rm He} = 0.3$. The actual ionization levels, mean molecular weight $\mu$, and specific energy $c_v$ are then obtained by assuming thermal balance and solving the appropriate Saha equations with all dissociation and ionization levels included. The pressure is given by the ideal gas law, $p = R_G\rho T/\mu$. The opacity $\kappa$ is approximated by the combined interpolation formulae as stated in Lin & Papaloizou (1985), which take into account additional species besides H and He and several chemical processes between them.

In most astrophysical disks, molecular viscosity is too small to provide a significant effect, and turbulent processes are generally assumed to be the driving mechanism for mass and angular momentum in disks (Pringle 1981). In the evolution equations above, it is assumed that the small-scale turbulence, caused for example by convective or MHD instabilities, acts macroscopically like a genuine viscosity. Thus, a frequently used expression for the disk viscosity is the $\alpha$ *Ansatz* (Shakura & Sunyaev 1973)

$$\nu = \alpha c_s H\,,$$

where $c_s$ is the sound speed, $H$ is the vertical height of the disk, and $\alpha$ is a dimensionless constant. The simple heuristic interpretation for this expression is a turbulence operating with efficiency $\alpha < 1$, having a maximum eddy size $H$ and maximum turnover velocity $c_s$. In an equatorial BL, the disk's thickness increases continuously as it joins smoothly with the star, and the radial pressure scale height becomes comparable to or smaller than that in the vertical direction. Then this simple prescription for the viscosity breaks down and has to be modified (Papaloizou & Stanley 1986). Another possible failure has been linked to supersonic radial infall and causality (Popham & Narayan 1992). Here we use the following generalization, which has already been employed in studying accretion onto a white dwarf (Kley 1991):

$$\nu = \alpha c_s H_p\,, \tag{8}$$

where $H_p$ is the local "two-dimensional" pressure scale height,

$$H_p = \frac{p}{|\nabla p|} = \left(\frac{1}{H_R^2} + \frac{1}{H_\zeta^2}\right)^{-1/2}.$$

The viscosity in equation (8) is given by the smaller of the directional pressure scale heights ($H_R$, $H_\zeta$), which is vertical in disk regions and radial in stellar regions. In disk midplane regions, where $H_p$ can be large, we limit it to $H$. In the optically thin regions above the disk, the disk temperature and pressure scale height are much larger than those in the midplane, and the prescription in equation (8) may no longer be appropriate since radiative losses may lead to an efficient decay of turbulence. For the optically thin regions, we adopt $\nu = 5\times 10^{12}\ {\rm cm^2\ s^{-1}}$, which is much smaller than the value of $\nu$ in the midplane. In the stellar envelope, equation (8) coincides with the heuristic expression given for the viscosity of a convective envelope if we assume an eddy size comparable to the radial pressure scale height and a turnover velocity of $\alpha c_s$ (see, e.g., Kippenhahn & Weigert 1990). As we will point out later in discussing the results, although equation (8) results in a continuous viscosity coefficient throughout the computational domain, it can nevertheless lead to problems within the stellar envelope, where some modification may be needed. Therefore, we also performed some comparison calculations with a constant kinematic viscosity coefficient throughout. The bulk viscosity is neglected, as is commonplace in calculations of accretion disks, because the shear contribution ($t_{R\varphi}$) is overwhelmingly large in disks.

## 3. NUMERICAL SIMULATION

In order to analyze the hydrodynamic flow in the BL region numerically, we adopt a finite difference scheme. In this scheme, the system of partial differential equations (eqs. [2]–[6]) is discretized on a fixed Eulerian grid. We use a staggered grid in which the scalar quantities, such as density and temperature, are located at the cell centers and the vector quantities at the cell interfaces. The finite difference numerical scheme is a mixed explicit (advection, force) and implicit (viscosity, radiation diffusion) method that was developed to study the boundary layer between accretion disk and white dwarf in cataclysmic variable stars (Kley 1989). The different terms are dealt with consecutively (operator splitting), and advection is treated with a monotonic transport algorithm that is accurate to second order in space (Hawley, Smarr, & Wilson 1984). The radiative diffusion part is solved with the flux-limited diffusion approximation (Kley 1989). For numerical convenience we use dimensionless units, where the unit of length is the stellar radius, $r_0 = R_*$, and the unit of time is the dynamical time of the star, i.e., the inverse of the Keplerian orbital velocity at the stellar surface, $t_0 = (R_*^3/GM_*)^{1/2}$, from which the unit of velocity follows as $v_0 = r_0/t_0$. The temperature unit is the virial temperature $T_0 = u_0^2/R_G$, and the unit of density is arbitrarily chosen to be $\rho_0 = 5\times 10^{-6}\ {\rm g\ cm^{-3}}$.

### 3.1. *Model Considerations*

The two-dimensional $(R, \zeta)$ computational domain $\mathcal{D}$ extends from a minimum radius *inside* the star, typically $R_{\rm min} = 0.9R_*$, to a maximum radius $R_{\rm max} = 5R_*$. For the inner boundary of the computational domain, the envelope region well below the surface has a sufficiently large density that it is unlikely to be perturbed by the disk. Thus, the local physical quantities derived from the standard stationary

stellar model at this location provide adequate inner boundary conditions. Numerical limitations render the obvious choice $R_{\rm min} = 0$ impossible. Instead, we select $R_{\rm min} = 0.9R_*$ on the basis that the gas density (of a 1 $M_\odot$ star) has reached $10^{-3}$ g cm$^{-3}$ (cf. $<10^{-7}$ g cm$^{-3}$ in the disk) at a temperature of $\sim 2 \times 10^5$ K. This condition leads to a gas pressure 6 orders of magnitude higher than that of the incoming accretion disk. The outer radius of $\mathscr{D}$ is chosen to be sufficiently large that the disk is not too strongly affected by the star. For lower accretion rates, where the disk stays thin ($H/R \sim 0.1$), $R_{\rm max} = 2R_*$ proves to be sufficient (Kley 1989), but for high accretion rates, where the disk and BL thickness may be a considerable fraction of the stellar radius, a larger extent is required. For direct comparisons, we choose $R_{\rm max} = 5R_*$ for all models. In the vertical direction the model extends from the equatorial plane $\zeta_{\rm min} = 0$ up to the polar axis $\zeta_{\rm max} = \pi/2$. The inclusion of the polar axis allows us to follow the movement of matter up to higher stellar latitudes. The flow is assumed to be symmetric about the equatorial plane, which may not be exactly the case if convective cells in the disk are odd (Kley, Papaloizou, & Lin 1993b), but for a study of the basic structure of the BL, this approximation is adequate. In the finite difference approximation, the computational domain is typically covered by $N_R(125) \times N_\zeta(85)$ grid cells. In the radial direction, the grid cells are concentrated near the stellar photosphere ($R = 1.0R_*$), i.e., the resolution decreases at larger radii, where the radial pressure scale heights are also increasing. The angular grid points are more densely spaced within the thermal scale height of the disk.

As initial conditions we impose, first, radially a stationary stellar structure model, which includes, in addition to the physics contained in equations (2)–(6), convective transport of energy. The constitutive relations are identical to the combined disk/star model. This initial stratification of the stellar envelope is obtained by using a gray stellar atmosphere code. This code solves the ordinary differential equations for $T(R)$ and $\rho(R)$ by a fourth-order Runge-Kutta method, integrating outward, varying the initial density to obtain $T = T_*$ at optical depth $\tau = 1$. These first-order equations are obtained from hydrostatic equilibrium and flux conservation:

$$\frac{dp}{dR} = -\frac{\rho G M_*}{R^2},$$

$$R^2(F_{\rm rad} + F_{\rm conv}) = \text{const} = R_*^2 \sigma T_*^4,$$

where the radiative flux is given by equation (7) and the convective flux is implemented as in Kippenhahn & Weigert (1990).

Outside the stellar photosphere we impose an accretion disk that extends from about $R = 1.05R_*$ to the outer boundary. The two-dimensional disk stratification has been obtained by the linear interpolation from one-dimensional vertical equilibrium models at the two radial locations $R = 1.05R_*$ and $R_{\rm max}$. The vertical models are calculated for a given mass-flow rate and viscosity, using again, for consistency, the same physics as in the two-dimensional calculations. The equations solved for these vertical models are vertical hydrostatic equilibrium and flux conservation:

$$\frac{dp}{dz} = -\frac{\rho G M_* z}{r^3},$$

$$\frac{dF}{dz} = \frac{9 G M_* \rho \nu}{4 r^3},$$

where $r$ is the cylindrical radius at which the model is calculated and $z$ is the vertical distance from the equatorial plane. These equations are solved by a one-dimensional, time-dependent hydrodynamic code that has relaxed to equilibrium (see Tschäpe & Kley 1993). By applying this setup procedure we ensure that the two-dimensional initial condition is approximately compatible with an equilibrium disk structure and is reasonably close to it.

As boundary conditions we apply symmetry conditions (vanishing gradients) on the polar axis and in the equatorial plane. The inner boundary ($R_{\rm min}$) is implemented as a rigid wall with a no-slip boundary, i.e., the velocity is given solely by the angular velocity of the star. The outer boundary (at $R_{\rm max}$) is divided into two parts. In the inflow region of the disk, the initial conditions of the disk are kept fixed, which ensures a constant mass-inflow rate into the domain. Above the disk, simple outflow conditions (zero radial gradients, no torques) are imposed. No inflow is allowed in this region.

### 3.2. *Model Parameters*

In this paper, we present the results for three models. All have the same central protostar, which has one solar mass and a size of $R_* = 3\ R_\odot$. The effective temperature of the protostar is $T_{\rm eff} = 4000$ K, which is equivalent to a luminosity of $3\ L_\odot$. To calculate the stellar envelope/atmosphere structure we assume that the gravitational potential is solely created by the central parts of the protostar, which here is a point mass of $M_* = 1\ M_\odot$. The incoming matter from the disk is assumed to be non–self-gravitating. The protostar rotates with 1/10 its breakup velocity, $\Omega_* = 0.1\Omega_K(R_*)$. This value corresponds to the observed values for protostars (Cohen & Kuhi 1979) and is dynamically unimportant for the flow structure. Given these stellar parameters, the disk's structure is determined by the viscosity and the mass-inflow rate. For the standard model (model 1), we adopt $\dot{M} = 10^{-6}\ M_\odot$ yr$^{-1}$, which corresponds to that derived from the spectral energy distribution of typical flat-spectrum T Tauri stars, such as HL Tau (Lin et al. 1994). We also consider a high-flux model (model 2) with $\dot{M} = 10^{-4}\ M_\odot$ yr$^{-1}$, which is appropriate for the outburst phase of FU Orionis stars (Hartmann et al. 1993). Finally, we examine a low-flux model (model 3) with $\dot{M} = 10^{-7}\ M_\odot$ yr$^{-1}$, which is comparable to the value inferred from emission lines of classical T Tauri stars (Strom, Kepner, & Strom 1995; Basri & Bertout 1993). The mass-inflow rate is fixed at the outer boundary at $R_{\rm max}$. For the constant viscosity parameter $\alpha$ we take $10^{-2}$ throughout.

## 4. THE STANDARD MODEL

Before we investigate the influence of a change in the mass-inflow rate, we will display the generic features of our two-dimensional analysis of accretion onto a protostar for a model with the standard parameters (model 1).

### 4.1. *Evolution toward a Quasi-Equilibrium State*

One-dimensional analysis of local vertical structure at a given radius indicates that the temperature in the inner regions of the disk is in a range such that the continuum opacity is dominated by the dissociation of molecular hydrogen and the disk is convectively unstable. At the onset of our two-dimensional computation, the disk undergoes a brief phase of rapid initial evolution in order to adjust to a new quasi-equilibrium. We followed the time evolution of the standard model for $\sim 3 \times 10^3$ dynamical times (at $R =$

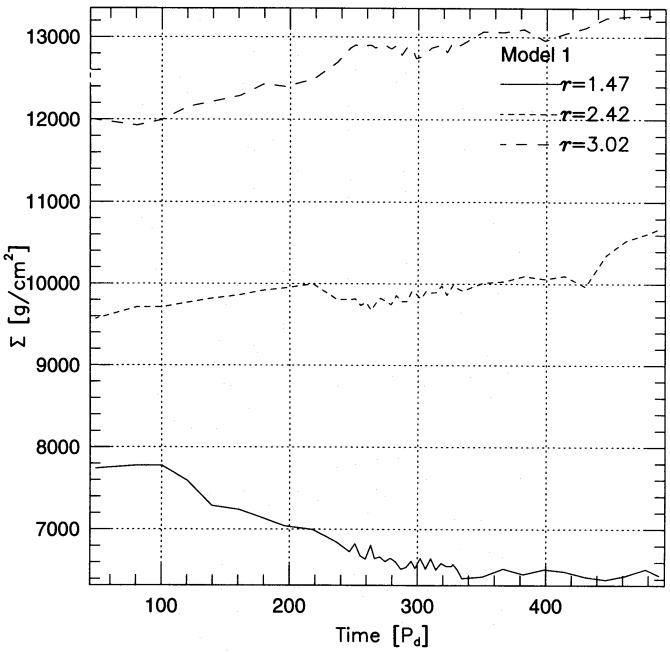


FIG. 1*a*

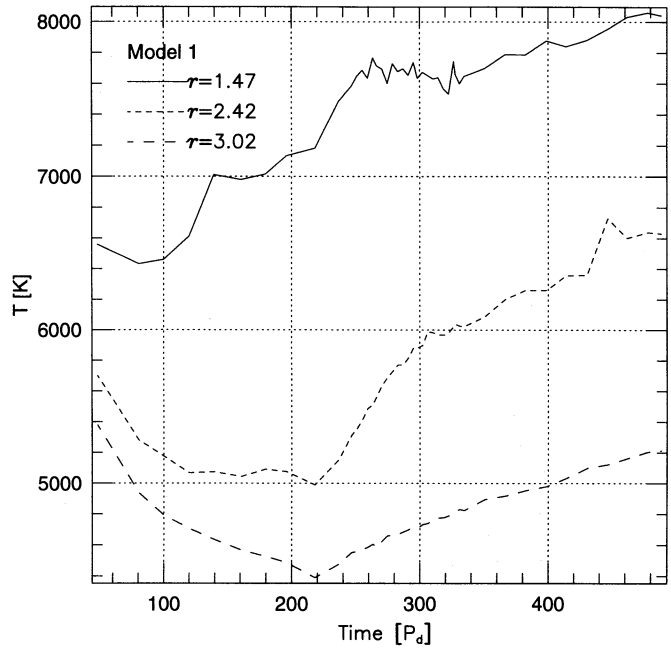


FIG. 1*b*

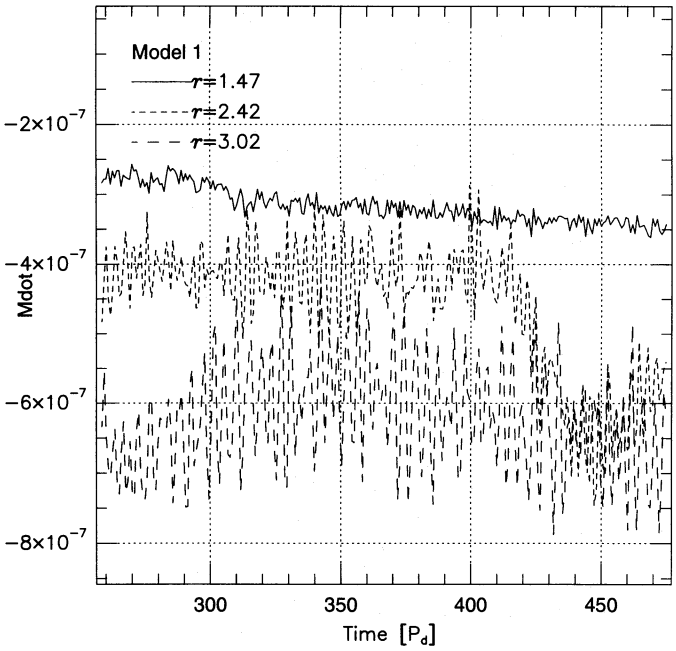


FIG. 1*c*

FIG. 1.—Time dependence of (*a*) surface density (g cm$^{-2}$), (*b*) central temperature (K) in the disk, and (*c*) the moving time average of the local mass-inflow rate ($M_\odot$ yr$^{-1}$) at three different radii for the standard model (model 1). The unit of time in this and all subsequent figures is the Keplerian orbital period $P_d$ at $R = R_*$.

$R_*$), which corresponds to $\sim 5 \times 10^2$ Keplerian orbital periods ($P_d$). In order to demonstrate that this timescale is sufficiently long for the system to come to a quasi-static equilibrium configuration, we plot in Figures 1*a* and 1*b* the surface density $\Sigma = \int_{-\infty}^{\infty} \rho\, dz$ and the midplane temperature $T_c$ at three radial locations, $R/R_* = 1.47$, 2.42, and 3.02. The surface density attains a quasi-equilibrium value within $10^2$ orbital periods and changes slowly thereafter, on much longer ($\sim 10^5 P_d$) timescales. The thermal structure of the disk changes somewhat faster, on timescales of $\sim 10^4 P_d$.

In Figure 1*c* the moving time average of the mass-influx rate $\langle \dot{M} \rangle = (2\,\Delta t)^{-1} \int_{t-\Delta t}^{t+\Delta t} \dot{M}\, dt$, with $\Delta t \sim 5P_d$, is displayed at the same radial loci. The small amplitude fluctuations in $\langle \dot{M} \rangle$ are induced by convection and overstable pulsation in the disk (see § 4.2). The amplitude of these fluctuations is much larger in the instantaneous mass accretion rates $\dot{M}$ ($= 2\pi \int_{-\pi/2}^{\pi/2} \rho R^2 v_R\, d\zeta$) than in the displayed average because the convective velocity is comparable to or larger than the diffusion speed. Despite these fluctuations, $\langle \dot{M} \rangle$ attains asymptotic mean values that are comparable to but somewhat smaller than the input mass flux. Consequently, mass gradually accumulates in the disk. The values of $\dot{M}$ at the three radial locations indicate that $\dot{M}$ increases with $r$, which is consistent with the slow secular increases of $\Sigma$ and $T_c$. The implication of this evolutionary tendency will be discussed in § 6 and elsewhere.

In order to demonstrate that an identical quasi-equilibrium structure may be obtained with completely different initial conditions, we introduce model 1a, which has identical model parameters as those of the standard model but in which the disk is initially placed beyond $R = 1.3R_*$. The inner boundary of the disk gradually diffuses toward the central star on the diffusion timescale [$\tau_d \simeq (\Delta r)^2/\nu \simeq (\alpha\Omega)^{-1}(\Delta r/H)^2$]. For model 1a, $H/r \sim 1/15$ and $\alpha = 10^{-2}$, so $\tau_d \sim 150P_d$ is required for the inner boundary to diffuse by $\Delta r \simeq 0.2R_*$. This analytic estimate is consistent with the numerical results in Figure 2, which show that the inner boundary of the opaque disk region reaches $r \sim 1.1R_*$ after $t \simeq 100P_d$ and stalls near there. After $t = 200P_d$, the disk structures of models 1 and 1a are essentially identical.

### 4.2. *Thermal and Kinematic Structure of the Disk*

We continued our calculation for several hundred orbital periods after the quasi-equilibrium was established. During this time there was no significant change in the global structure of the disk. In Figure 3, we plot the velocity vectors at $t = 488P_d$ at alternating radial zones superimposed onto the density distribution in the disk. Convective flow pattern is clearly visible in both the disk and stellar envelope. While

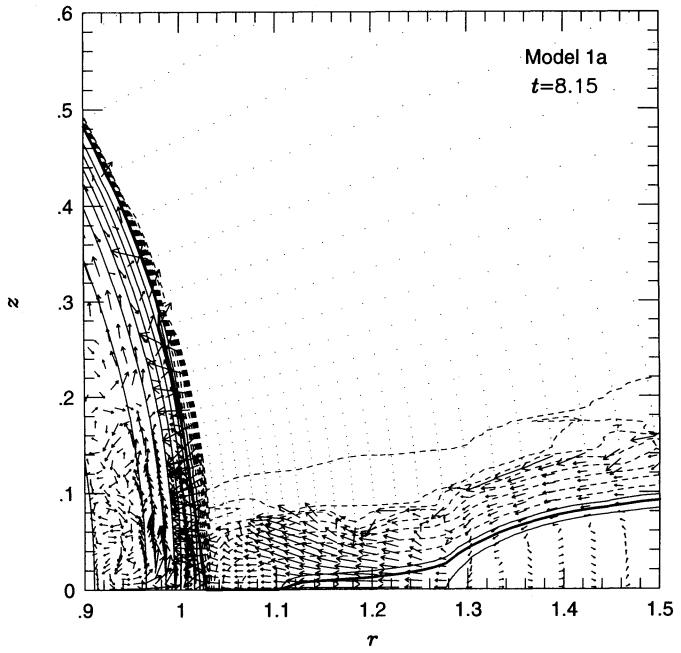


FIG. 2a

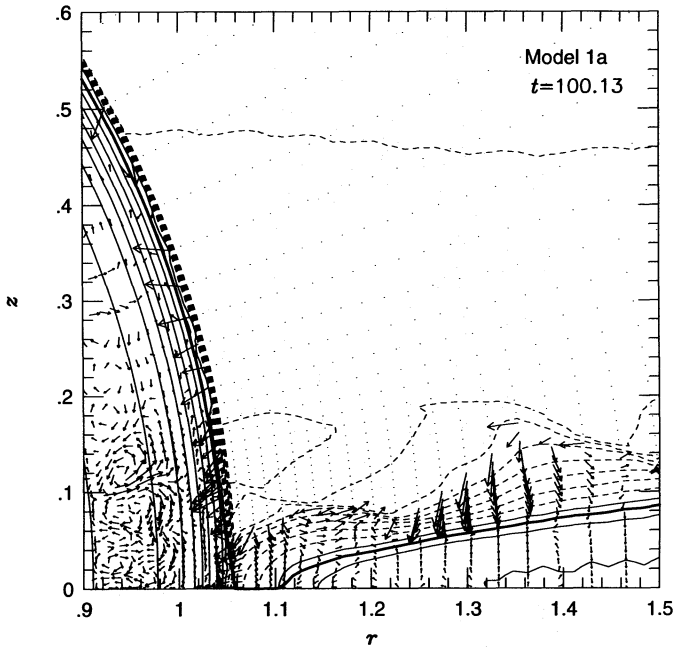


FIG. 2b

FIG. 2.—Results for model 1a, showing density contours and velocity vectors. Solid contours indicate larger values of $\rho$ while dashed contours denote smaller values. The disk was initially placed at radii greater than $1.3R_*$; viscous action causes a rapid inflow. The approximate $\tau = 1$ surface is shown by the thick solid line. Displayed is the inner part of the computational domain.

in the stellar envelope the flow field is rather complicated, with convective eddies elongated more in the radial direction, in the disk the eddies are elongated exclusively perpendicular to the midplane. Since many dynamical timescales are needed to establish a quasi-equilibrium state, we use only 125 radial zones in our difference scheme so that asymptotic numerical solutions may be obtained on realistic computational timescales. The extent of each radial zone is $\Delta R \sim 0.015R \sim 0.2H$. The largest eddies are only marginally resolved since their radial width is covered only by a few ($\sim 3$) zones; in the vertical direction, though, they span several ($\sim 15$) zones. In principle, the structure of the convective eddies may be affected by the numerical viscosity due to the coarse resolution. However, the effective viscosity we have introduced with the $\alpha$ prescription also suppresses the small-scale eddies (Kley et al. 1993b). Provided the specified viscosity dominates the numerical viscosity, the statistical properties of the convective eddies and the structure of the disk should not be strongly affected by the limited numerical resolution. In order to verify this conjecture, we carried out a modified computational model in which all the physical parameters were identical to the standard model. In the modified model, we used 80 radial zones to cover a region between $R_{\min} = 0.9R_*$ and $R_{\max} = 2R_*$ such that $\Delta R = 0.01R$. Despite the difference in the spatial resolution, there was no significant difference between these two models.

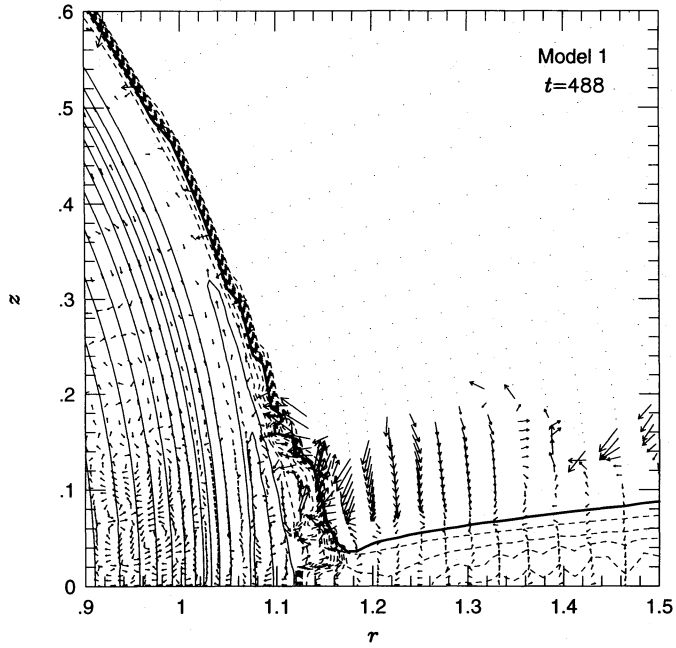


FIG. 3.—State of model 1 at the final time, $t = 488P_d$. The disk has made contact with the star and created an equatorial belt. The convective motions in the disk and star are clearly visible.

Although the convective speed is subsonic (typical velocities are $v_{\rm conv} \sim \alpha c_s$), it is much larger than the mean diffusion speed $[v_r \sim \alpha(H/r)c_s \sim 10^{-3}c_s]$. Thus, convection introduces a large fluctuation in the instantaneous mass flux $\dot{M}$ (see Fig. 1*c*). Because typical eddies persist on a turnover timescale that is a fraction of $P_d$, the fluctuation amplitude in the moving time average $\langle \dot{M} \rangle$ is much reduced from that in $\dot{M}$.

In Figure 3, we also highlight the location of the photosurface of the disk, where the opacity is $\tau = 1$ (*thick line*). The thickness of the disk is $H \sim 0.06r$ for $r > 1.3R_*$, which is in agreement with that derived from the local vertical-structure calculations (Lin & Papaloizou 1980, 1985). But near the inner boundary of the disk, adjacent to the central star, the photosurface expands from the midplane before joining smoothly with the protostar.

### 4.3. *Validity of Vertical-Averaging Approximation*

In disk evolution calculations, it is convenient to adopt a thin-disk approximation (Shakura & Sunyaev 1973), in

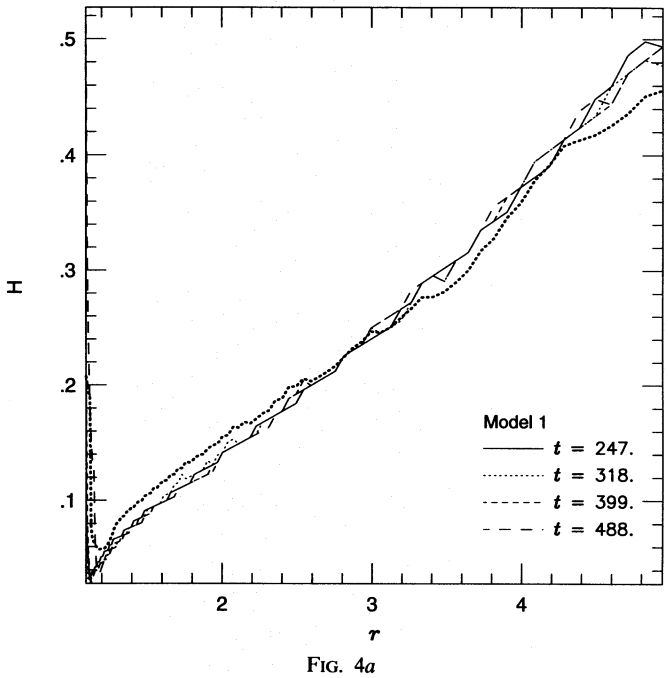


FIG. 4a

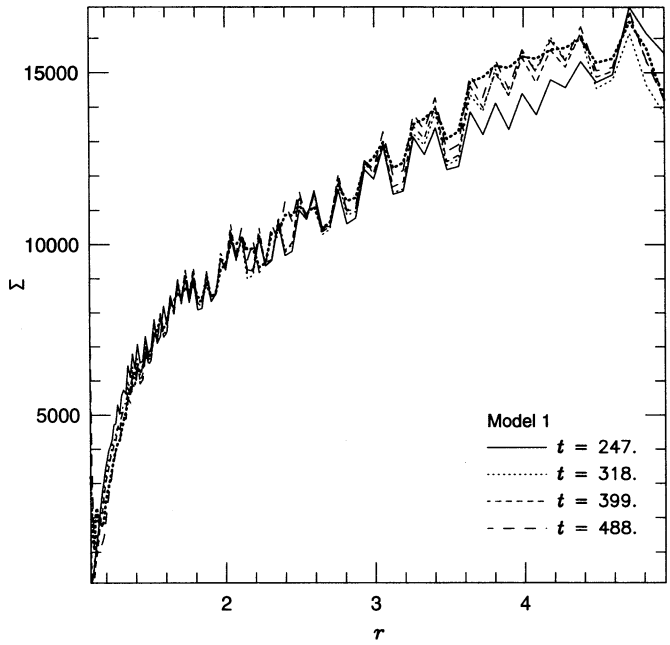


FIG. 4b

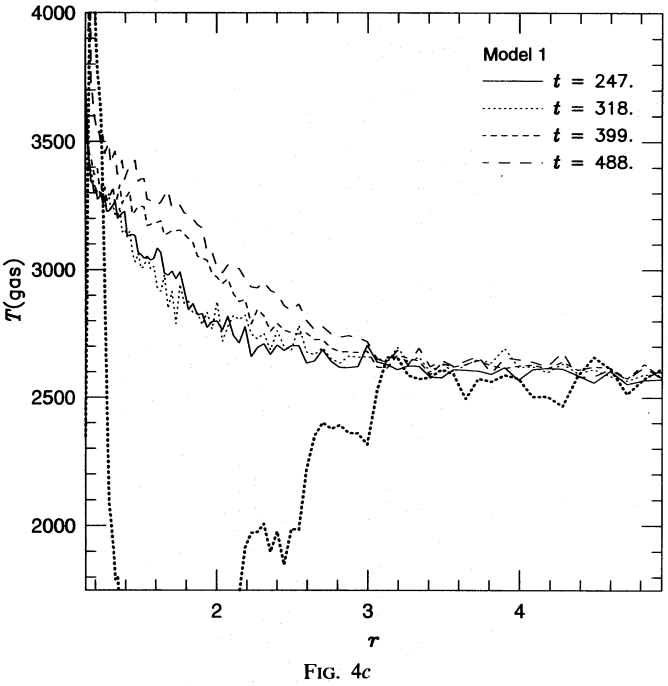


FIG. 4c

FIG. 4.—(*a*) Height of the $\tau = 1$ surface, (*b*) surface density (g cm$^{-2}$), and (*c*) midplane gas temperature (K) at four different times for model 1. The thick dotted lines represent the values of the one-zone thin-disk approximation (see § 4.3).

which the disk's half-thickness, $H_1 = f_H c_s(z = 0)/\Omega$, the surface density, $\Sigma_1 = f_\Sigma 2H_1\rho_c$, and the effective surface temperature, $T_e = f_T T_c/\tau^{1/4}$, are expressed as functions of the midplane density $\rho_c$, midplane temperature $T_c$, and total optical depth $\tau = \int_0^\infty \kappa\rho\, dz \sim \Sigma_1\kappa_c/2$. The normalization constants $f_H$, $f_\Sigma$, and $f_T$ are of order unity. This approximation is adequate for all regions except where the opacity ($\kappa$) increases rapidly with $T$ (Faulkner, Lin, & Papaloizou 1983). In the standard model, $T > 2 \times 10^3$ K near the inner boundary of the disk such that $\kappa$ is dominated by molecular and $H^-$ processes and is an increasing function of $T$.

In Figure 4, we compare $z(\tau = 1)$ with $H_1$, $2\int_0^\infty \rho_c\, dz$ with $\Sigma_1$, and $T(\tau = 1)$ with $T_e$, using the normalizations $f_H = 2$, $f_\Sigma = 1.33$, and $f_T = 2.2$. The thin-disk approximations are given by the thick dotted lines, and the numerical results at different times by the thinner lines. Although the slope of $H_1(r)$ deviates slightly from the two-dimensional numerical result, the overall agreement of the one-zone model and the two-dimensional model in the first two cases is very good, i.e., the thin-disk approximation adequately describes both $H$ and $\Sigma$, using appropriate normalization factors. However, it is a poor approximation for the temperature distribution. Since $T_e$ determines the spectral energy distribution, there may be a potential difficulty with the one-zone BL models.

### 4.4. *Mass, Angular Momentum, and Heat Transport*

In § 4.2 we indicated that both convection and overstable pulsation induce time-dependent variations in $\dot{M}$ at any given radial location. In Figure 5, we show that the primary effect of convection is confined to the inner disk at $r < 3R_*$, where the amplitude of variation in $\dot{M}$ is small and comparable to the infall flux ($\sim 10^{-6}\ M_\odot\ \mathrm{yr}^{-1}$). In contrast, the overstable pulsation is effective at $r > 3R_*$ and induces large-amplitude ($> 10^{-4}\ M_\odot\ \mathrm{yr}^{-1}$) $\dot{M}$ variations. The criterion for pulsational overstability depends on the functional form of the viscosity prescription (Kley et al. 1993a) and, in this particular case, on the existence of a reflecting outer boundary. Thus, its occurrence in nature remains questionable (see also Papaloizou & Stanley 1986). These results are consistent with the high-resolution calculations of convectively unstable protoplanetary disks (Kley et al. 1993b).

The radial oscillations also carry angular momentum with the fluid. In Figure 5*c*, we plot the advective angular momentum flux $\dot{J}_{\mathrm{adv}} = 2\int_0^\infty \rho v_r \Omega r^3\, dz$, which is much larger than that due to viscous stress ($\dot{J}_{\mathrm{vis}}$; Fig. 5*d*). However, $\dot{J}_{\mathrm{adv}}$ is mostly carried by the oscillating fluid elements in the convective or pulsating eddies. Only a small fraction of $\dot{J}_{\mathrm{adv}}$ (carried by the inwardly diffusing gas) actually contributes to the secular redistribution of angular momentum. In a

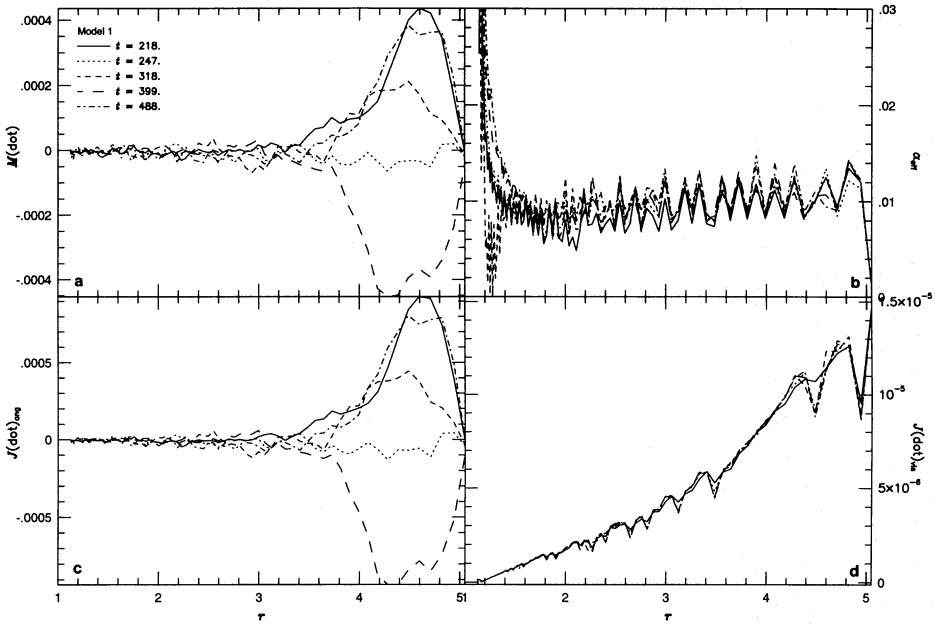


FIG. 5.—(*a*) Mass-flow rate ($M_\odot$ yr$^{-1}$), (*b*) effective $\alpha$, (*c*) advective angular momentum flow (g cm$^2$ s$^{-2}$), and (*d*) viscous angular momentum flow (g cm$^2$ s$^{-2}$) at five different times for model 1.

stationary situation the sum of advective and viscous angular momentum flux is constant and equals the accreted angular momentum of the star.

In a Keplerian disk in equilibrium, the assumption of local release of the dissipated energy (see also below) reads $F_s = \int_0^\infty \Phi\, dz = (9/4)\Omega_K^2 \int_0^\infty \eta\, dz$, where $F_s(r)$ is the radiative flux emitted from the disk's surface at radius $r$. A useful quantity to measure the departure from this equilibrium (let us call it the "viscous effect") is $\alpha_{\rm eff} = 4F_s\alpha/(\int_0^\infty \eta\, dz\, 9\Omega_K^2)$, which is plotted in Figure 5*b*. This effective $\alpha$ also gives some indication of the efficiency of angular momentum transport in the disk in relation to the usual thin-disk approximation. Here, in equilibrium, $\alpha_{\rm eff}$ equals exactly the imposed value of 0.01. Only in the BL region is there an excess of radiative flux, because of the breakdown of the thin-disk approximations. In addition, in nonstationary situations $\alpha_{\rm eff}$ may differ considerably from the nominal value.

An important assumption of the thin-disk approximation is that the energy dissipated is radiated locally. In Figure 6, we plot the rate of viscous energy dissipation ($D_v = \int_0^{\pi/2} \Phi R\, d\zeta$, where $\Phi$ includes all terms from the viscous stress tensor; see § 2) and the radiative flux at the surface [$F_s = f_\zeta(\tau = 1)$], and compare them to the advective thermal energy transport [$F_{\rm adv} = \int_0^{\pi/2} e_{\rm th}(\partial v_R/\partial R)R\, d\zeta$] and radiative flux ($F_r = \int_0^{\pi/2} F_R R\, d\zeta$) in the radial direction. Throughout, both $F_{\rm adv}$ and $F_r$ are much smaller than $F_s$ and $D_v$, another indication that local thermal equilibrium is established. In the inner part the contributions of advection and radial flux are slightly larger, but still much less than $F_s$ and $D_v$. Large values of $F_{\rm adv}$ would imply that (radial) convection dominates the heat transport. Previous analyses showed that although convective heat transport in the disk is negligible when $\alpha \sim 1$ (Tayler 1980; Faulkner et al. 1983), it may become important for small values of $\alpha$ (Cannizzo & Wheeler 1984; Kley et al. 1993b).

### 4.5. *Boundary-Layer Flow*

In the BL interface between the star and the disk, $\Omega$ changes rapidly from its value at the stellar surface to near the local Keplerian value $\Omega_K = (GM_*/r^3)^{1/2}$ (Fig. 7*a*). This transition occurs over a radial scale $\sim 0.05R_*$, which does not change with time. Using the appropriate values for the effective viscosity, the boundary thickness obtained here is comparable to those estimated on the basis of simple analytic approximations (Lynden-Bell & Pringle 1974) and one-dimensional numerical solutions (Popham & Narayan 1991).

As a consequence of losing centrifugal balance, gas in the BL accelerates toward the central star with radial velocity $v_R$ much larger than that associated with viscous diffusion

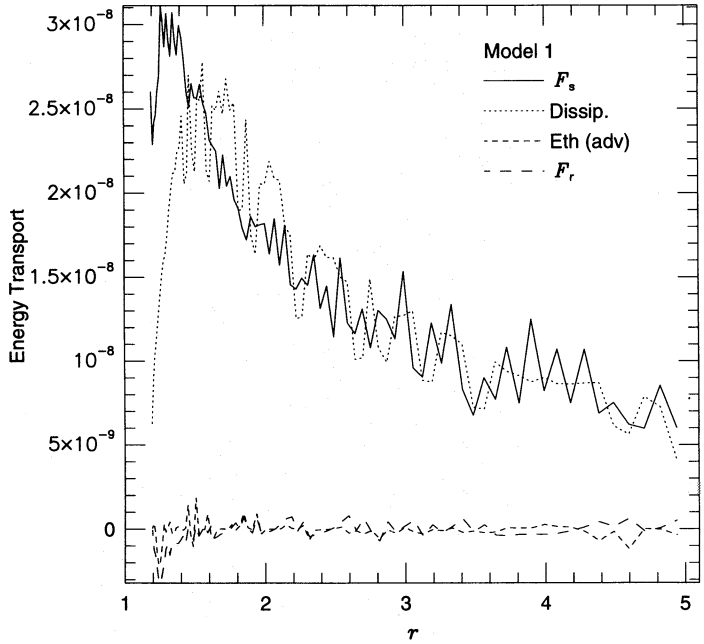


FIG. 6.—Local energy balance of the disk. Displayed are the surface flux $F_s$ emitted from the disk (*solid line*), vertically integrated dissipated energy (*dotted line*), vertically integrated advected thermal energy (*short-dashed line*), and radial diffusion of radiative energy $F_r$ (*long-dashed line*) for model 1. The unit of the energy flux is g cm$^{-1}$ s$^{-3}$.

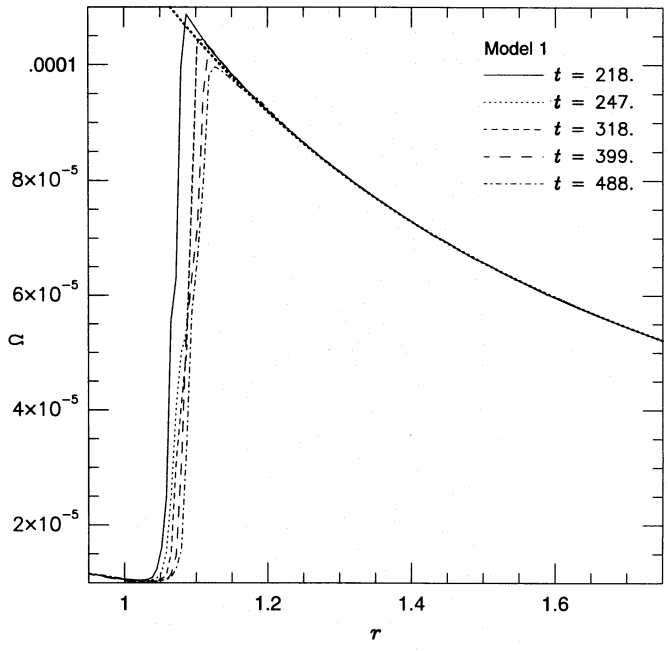


FIG. 7a

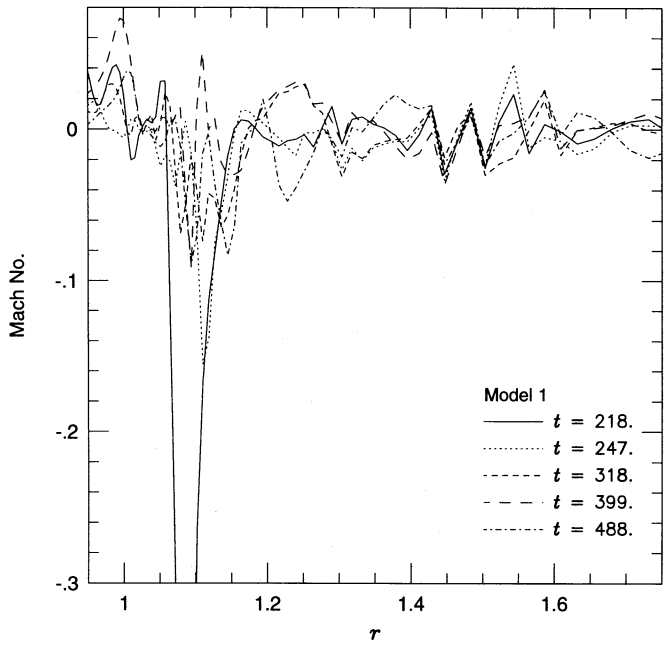


FIG. 7b

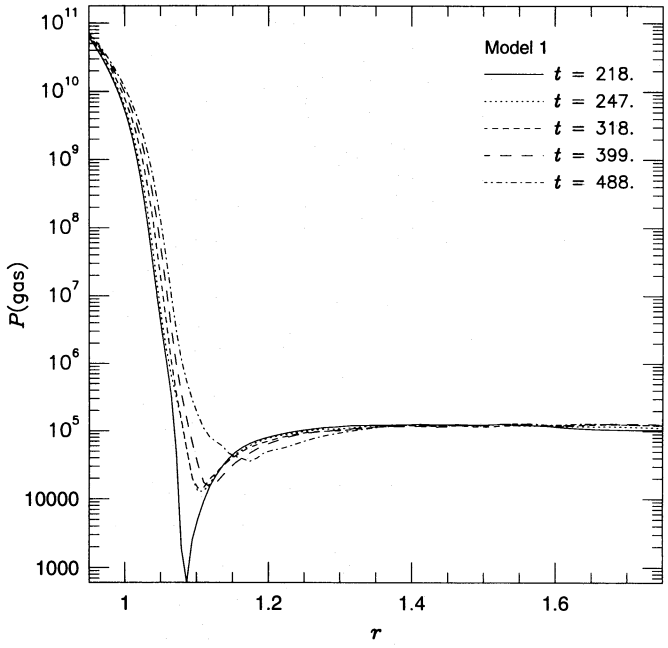


FIG. 7c

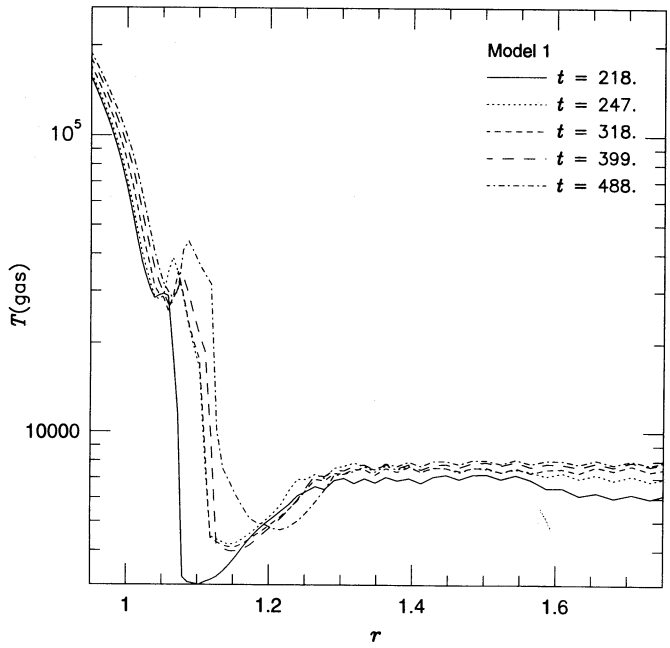


FIG. 7d

FIG. 7.—(*a*) Angular velocity ($s^{-1}$), (*b*) radial Mach number, (*c*) pressure (g $cm^{-1}$ $s^{-2}$), and (*d*) temperature (K), all taken at the disk midplane, for model 1. In (*a*) the thick dotted line denotes the Keplerian value.

$[\alpha(H/R)c_s]$ at $R \gg R_*$. Nevertheless, the Mach number, $M_c = v_R/c_s$, is generally less than unity (Fig. 7*b*), which satisfies the "causality condition" (Popham & Narayan 1992). The mass-infall rate onto the central star is maintained at a steady rate such that the large infall velocity also leads to a depletion in the local density in the BL. Consequently, there is a density minimum (see also Fig. 3). The pressure gradient in the small region beyond the density minimum is positive and large (Fig. 7*c*). In order to compensate for the inwardly pointing pressure force, $\Omega$ has to slightly exceed $\Omega_K$ when the central balance is reestablished (Fig. 7*a*). This effect has already been noted by Popham & Narayan (1991).

Figure 7*d* illustrates the temperature distribution in the midplane. Deep in the stellar envelope, it decreases with radius and reaches a local minimum at $R \sim 1.08R_*$, followed by an inversion layer that attains a maximum temperature of $10^5$ K at $R \sim 1.092R_*$. Beyond this maximum, $T$ again decreases with radius. The maximum is caused by the strong dissipation in the BL, where $\partial\Omega/\partial R > 0$. This additional heating mechanism raises the temperatures above that of the surrounding envelope. This $T$ inversion is artificial in the sense that the initial temperature distribution of the stellar envelope has been taken to be the undisturbed stellar thermal stratification, neglecting the contribution from the BL. On timescales of $\sim 10^7 P_d$ we

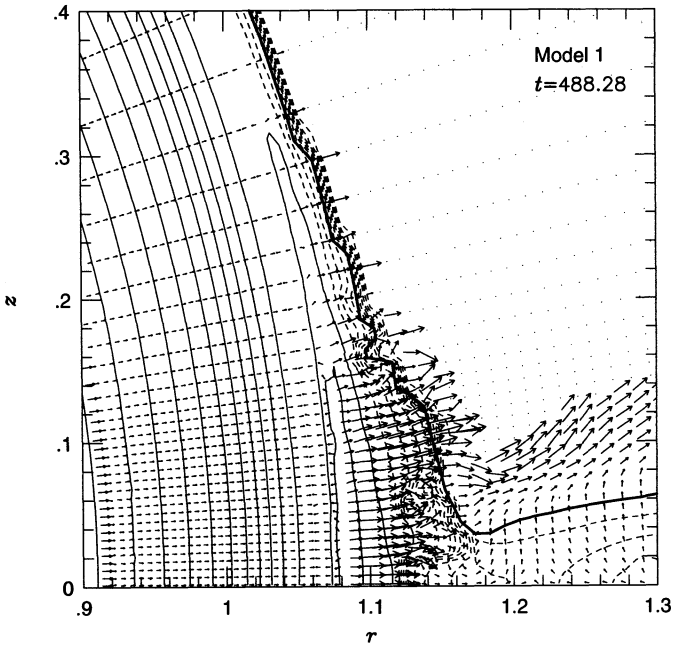


FIG. 8.—Blow-up of the inner region of model 1 at the final computed time. Displayed are temperature contours with radiative-flux vectors.

expect thermal adjustment to result in a monotonic $T$ stratification. This local maximum of the temperature is also clearly visible in the isotemperature contours and radiative-flux vectors in Figure 8. In the immediate interior of the temperature "ridge" near $R \sim 1.09R_*$ the radiation flux is directed inward, and it is directed outward in the exterior.

### 4.6. *Mass and Energy Flow in the Stellar Envelope*

A fine-resolution display of the flow pattern indicates that the inflow velocity in the BL region is comparable to the convective speed (Fig. 9). Thus, the fluctuation in $\dot{M}$ is relatively small. Interior to the BL, disk matter continually arrives onto a relatively thin zone in the envelope around the star's equator. For the duration of our computation, the mass, angular momentum, and thermal energy carried by the accreted material are much smaller than those in the stellar envelope, so the density and temperature structure of the stellar envelope are not significantly modified, as can easily be seen from the undisturbed spherical contour lines of temperature (Fig. 8) and also density (Fig. 9). Below the BL, the energy generated near the BL is smaller than that emerging from the base of the envelope, and the envelope remains convective. On a long timescale ($>10^8 P_d$), the material accreted via the equatorial region accumulates a mass comparable to the mass of the upper envelope. In order to maintain hydrostatic equilibrium, this matter must be redistributed over the entire surface. With the present numerical scheme, we cannot follow the flow pattern on such a long timescale.

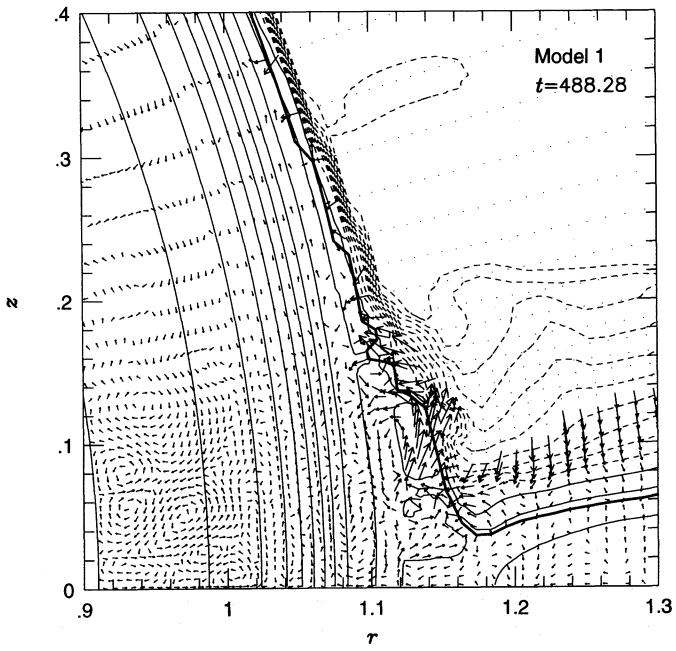


FIG. 9.—Blow-up of the inner region of model 1 at the final computed time. Displayed are density contours with velocity vectors.

### 4.7. *Spectral Energy Distribution and Disk Corona*

In the optically thin regions surrounding the BL, the radiative flux increases with the optical depth. Temperatures in these regions increase when the radiative flux is inadequate to dispose of the thermal energy generated through viscous dissipation. When the temperature becomes greater than $10^4$ K, $\kappa$ (and therefore the radiative flux) decreases with $T$. Further temperature increases can lead to the formation of a hot corona (see Fig. 8; see also King & Shaviv 1984; Kley 1989; Murray & Lin 1992). Since we are dealing here with a one-temperature approximation, the results show no indication of a hot corona above the disk. The continuum spectrum of the radiation emerging from the disk has been computed under the assumption of a locally blackbody temperature (Fig. 10).

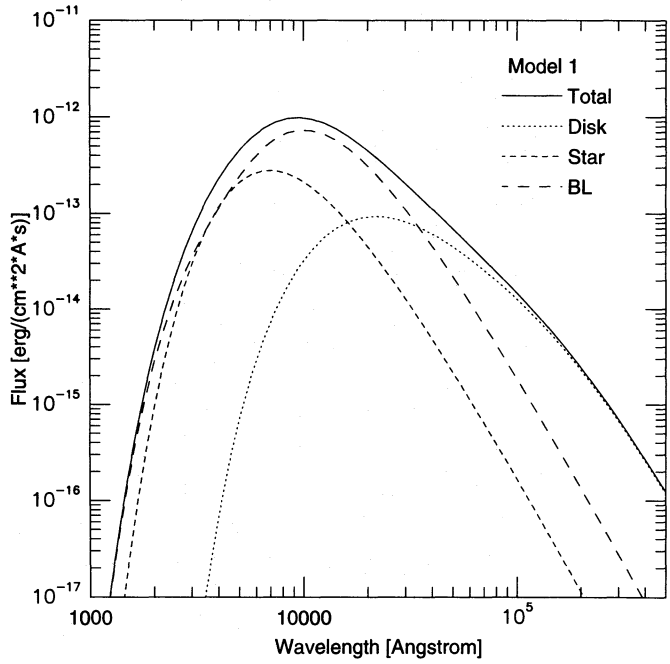


FIG. 10.—Spectral energy distribution for the final state of model 1. The spectrum was obtained by computing the $\tau = 1$ surface of the star/disk system, integrating over $T(r, H)$ assuming locally blackbody temperatures and using an inclination of 40° and a limb darkening of 1.5. The star reaches to $R = R_*$, the BL from $R_* < R < 5R_*$, and a model disk has been added outside that reaches up to $R = 100R_*$. The flux has been normalized to a distance of 100 pc.

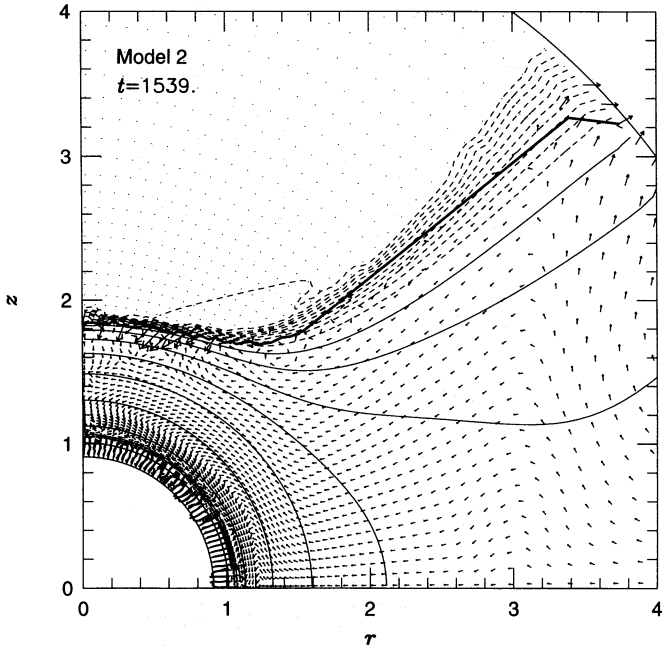


FIG. 11.—Density contours and velocity vectors for the final model 2

## 5. DEPENDENCE ON MASS FLUX AND VISCOSITY

Since there is a variety of mass-infall flux onto protostellar disks, we consider two limiting models. In addition, in order to evaluate the range of uncertainties associated with the poorly known viscosity, we vary the magnitude of and prescription for the viscosity.

### 5.1. *High-Flux Model*

For the high-flux model (model 2), we adopt a mass-infall flux of $10^{-4}\ M_\odot\ \mathrm{yr}^{-1}$. All other model parameters are identical to the standard model.

*Evolution toward a steady state.*—Since the energy-dissipation rate increases with $\dot{M}$, the disk temperature everywhere is much hotter in this case than in the standard model. The density distribution shows that the photosurface has a height $H \sim r$ for $r > 2R_*$ (Fig. 11). Inside this region, the isodensity contours become approximately spherically symmetric. Consequently, the magnitude of viscosity according to the $\alpha$ prescription becomes very large, and a very slowly varying quasi-stationary state is attained at $t < 50P_d$. To study the further long-term evolution, we continued our computation until $t \sim 1500P_d$. The density distribution and velocity vectors in Figure 11 are plotted for that final time. On this long timescale, the disk still undergoes minor secular adjustments, and we estimate the model will reach a stationary state approximately on a timescale of $10^4 P_d \sim 10$ yr. In Figure 12, we plot the midplane quantities, $\rho_c$, $T_c$, $\Omega_c$, and the radial Mach number $M_c$, at four epochs. During the evolution the thickness of the BL is still increasing, as indicated by the change in position of the maximum of $\Omega$ with time (Fig. 12*c*). This is accompanied by increases in $\rho$ and $T$ (Figs. 12*a*, 12*b*). It is customary to define the width of the BL by the radial location $d_{\max}$ where $\Omega$ attains its maximum value. The results in Figure 12 indicate $d_{\max} \sim 1.8R_*$ at the final time. This value falls between those deduced for $\alpha = 0.1$ ($1.2R_*$) and $10^{-3}$ ($>1.8R_*$) by Popham et al. (1993) using a thin-disk approximation. In the BL region, the value of $\Omega$ is considerably smaller than the local $\Omega_K$. However, the radial velocity (Fig. 12*d*) remains small ($M_c \simeq 10^{-4}$) because of the large outward pressure gradient in the radial direction; i.e., in this case the BL is primarily hydrostatically supported.

Following our discussion in § 4, we utilize the information on the radial distribution of $\dot{M}$, $\dot{J}_{\rm vis}$, and $\dot{J}_{\rm adv}$ (Fig. 13) to demonstrate that, apart from the persisting long-term evolution, the disk has evolved into a quasi-stationary steady state. All of these quantities are integrated along the line of constant spherical radius $R$ in the vertical direction. At $t = 700P_d$, the averaged mass-inflow rate has become constant with radius and equals the nominal inflow rate of $\dot{M} = 10^{-4}\ M_\odot\ \mathrm{yr}^{-1}$. Thus, the disk ceases to accumulate or deplete mass on both global and local length scales. Interior

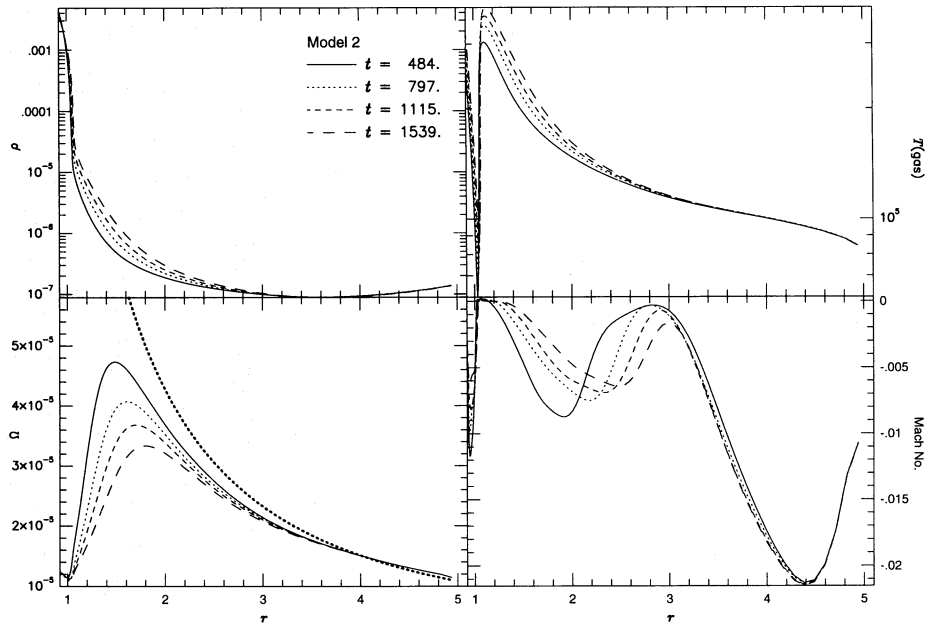


FIG. 12.—(*a*) Density (g cm$^{-3}$), (*b*) temperature (K), (*c*) angular velocity (s$^{-1}$), and (*d*) radial Mach number, in the midplane of the disk, for model 2 at four different times.

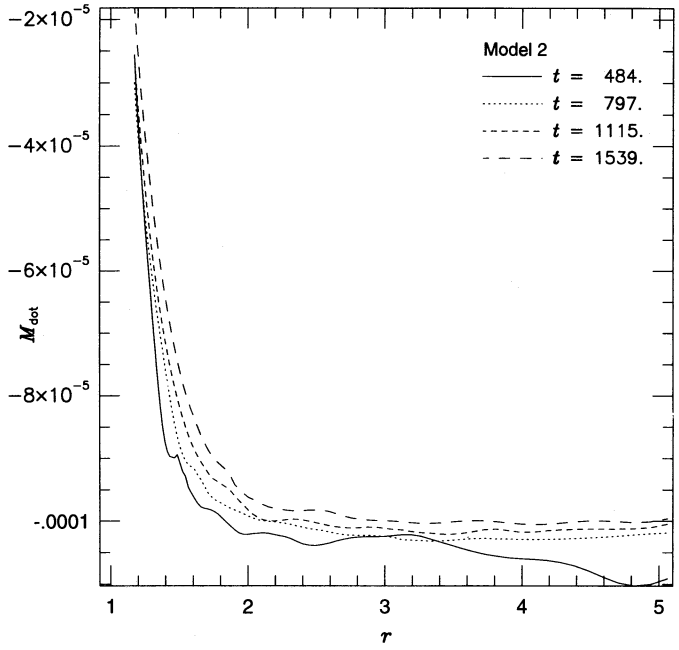


FIG. 13*a*

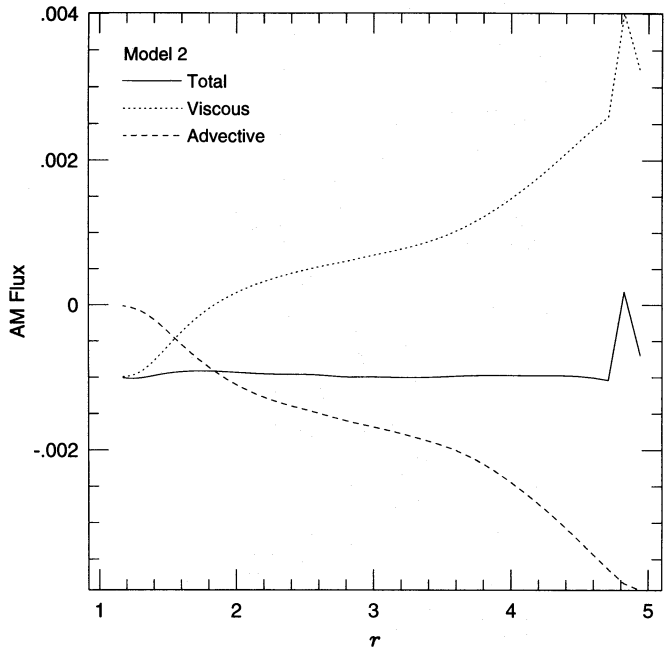


FIG. 13*b*

FIG. 13.—(*a*) Mass-inflow rate ($M_\odot$ yr$^{-1}$) at four times and (*b*) angular momentum flux balance (dimensionless units) at the final time, $t = 1539P_d$, for model 2.

to $r = 2R_*$, the flow significantly departs from the Keplerian flow, and a significant fraction of the accreted material is accreted near the polar region. The viscous and advective angular momentum fluxes are smooth and monotonic, and the total negative angular momentum flux $\dot{J}_{tot} = \dot{J}_{adv} + \dot{J}_{vis}$ is constant with radius (Fig. 13*b*), as to be expected in stationary situations. For the ratio $j$ of the accreted angular momentum to the specific angular momentum,

$$j = \frac{\dot{J}_{tot}}{\dot{M}\Omega_K(R_*)R_*^2}, \tag{9}$$

we find in this case $j = 0.87$. In one-dimensional stationary BL models, $\dot{J}_{tot}$ or $j$ serves as the second eigenvalue in addition to $\dot{M}$ in determining the solution (see, e.g., Narayan & Popham 1994). If we express the maximum value of the rotational angular velocity as $\Omega_{max} = \beta\Omega_K(r_{max})$ (Kley 1991) and note that the derivative of $\Omega$ vanishes at $r_{max}$, we find

$$j = \beta\sqrt{\frac{r_{max}}{R_*}}.$$

This relation is also numerically verified, e.g., by analyzing Figure 12*c*. Although $\beta$ is decreasing with time, the location of the maximum is increasing such that for all times displayed in Figure 12*c* the value of $j$ is identical. In standard disk theory one assumes that $\beta = 1$ or $j = 1$.

*Kinematic structure and thermal stratification.*—In contrast to the lower $\dot{M}$ standard model, the disk is fully ionized with $T_c > 10^5$ K at $r < 3R_*$ (Fig. 12*b*). This region is purely radiative because $\kappa$ decreases with $T$ (Lin & Papaloizou 1980; Faulkner et al. 1983). In the absence of convection, the poloidal ($r$, $z$) component of the velocity vector is directed radially inward between $r/R_* = 1.5$ and 3 (Fig. 11). In this region, the disk is pressure and rotationally supported such that these components are small compared with the local Keplerian speed. Interior to $1.5R_*$, gas in the disk flows around the stellar surface, engulfing the entire star. The only departure from laminar flow occurs near the outer boundary at $R_{max}$ and is caused by the boundary conditions.

*Heat flux along the radial direction.*—It is self-evident that the thick disk structure in Figure 11 cannot be adequately described by the local thin-disk ($H \ll r$) approximation, in which $\Omega$ is assumed to be a function of $r$ only. Outside $r = R_*$, the temperature scale height in the vertical direction is $\sim r$ (Fig. 14). Near the stellar surface, the temperature distribution also becomes approximately spherically sym-

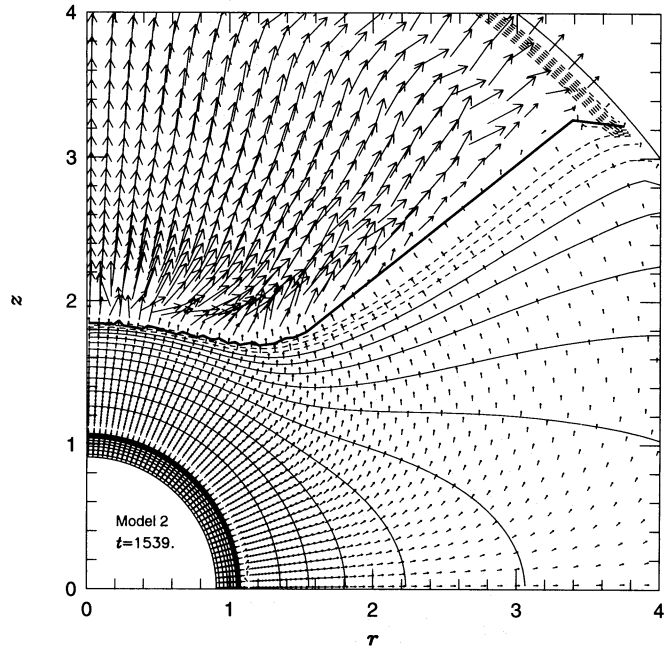


FIG. 14.—Temperature contours and radiative-flux vectors for the final model 2.

metric. Thus, the radiative flux is no longer directed primarily perpendicular to the disk's midplane. In contrast to the standard model, the flux near the midplane is directed mostly in the positive radial direction. The radiative flux in the radial direction generally dominates the advective heat transport carried by the inward-flowing gas. For the temperature range, bound-free and bremsstrahlung processes dominate the opacity such that $\kappa$ decreases with $T$. Thus, the amplitude of the flux is larger near the midplane. This efficient radiation transport in the radial direction is responsible for redistributing the heat dissipated in the BL throughout the inner regions of the disk. Consequently, it is the main cause of the difference in $H$ between the present computation and that obtained on the basis of the one-dimensional thin-disk approximation (Popham et al. 1993).

In our computation, we imposed an isolated stellar model as the initial condition for the accreting star. The photosphere of the star was initially located at $R = 1.0R_*$. Since the accreting star is embedded by the inner region of the disk, radiation can no longer escape from its surface freely. By $t = 1500P_d$, the photosphere has expanded to $R = 1.8R_*$. In the disk, the nonlocal heat transport redistributes the energy dissipated over an extended surface area such that the effective temperature does not change rapidly with the disk's radius. In Figure 15, we plot the theoretical continuum blackbody spectrum. For the plot, the BL thickness is located at the minimum height of the star/disk system, i.e., at $R \sim 1.3R_*$. The maximum of the spectral energy distribution is shifted to shorter wavelengths. As the transition between the BL and the star is somewhat confused, there is no distinct signature of the boundary layer.

*Flow in the stellar envelope.*—Gas flow from the disk onto the stellar envelope is best illustrated by the close-up $\rho$-$v$ distribution in Figure 16, which is an amplified version of Figure 11. As a consequence of viscous stress, $\Omega$ increases with $r$ below the BL. The intense dissipation leads to a local temperature maximum ($T_{\max} \sim 3 \times 10^5$ K). Since the gas density in the stellar envelope and atmosphere decreases rapidly with radius, $\Omega$ is brought to the stellar rotation rate

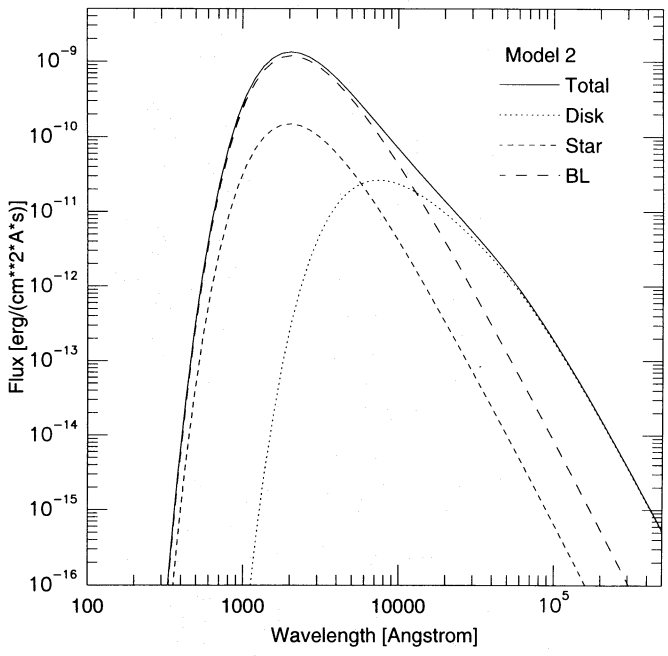


FIG. 15.—Spectral energy distribution for model 2

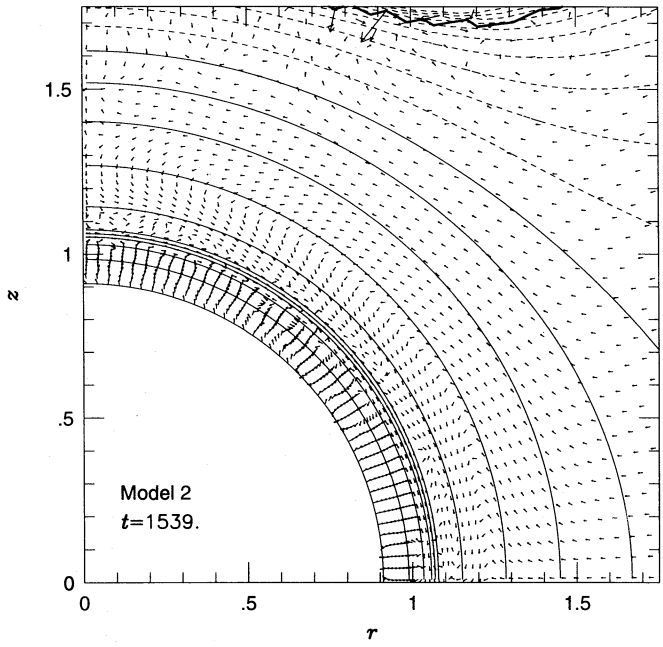


FIG. 16.—Density contours and velocity vectors in the inner regions for the final model 2.

such that the viscous dissipation quickly vanishes below the interface. The incoming material from the thick disk does not only reach the star near the equator but engulfs the whole star. In the transition region $R \simeq 1.08R_*$ to $R \simeq 1.2R_*$ (note that the stellar surface here is approximately at $R = 1.08R_*$; see discussion in § 5.2), where the incoming gas makes contact and mixes with the original stellar material, the latter is spun up, and an Ekman flow from the pole toward the equator is induced in this region. Below the transition zone, however, the accreted material has little impact on the dynamical structure in the stellar interior. Convection patterns continue to dominate the structure of the envelope.

The surface temperature of the star is initially $4 \times 10^3$ K, which is much less than the maximum dissipation temperature $T_{\max}$. Thus, the temperature gradient is negative in the stellar interior and positive in the transition zone (cf. also Fig. 12*b*). This temperature distribution induces a radiative flux from the stellar interior as well as the BL to the location of the temperature minimum. Inside the envelope the radiative diffusion timescale $t_{\rm diff}$ is of the order $\sim 10^7 P_d$, and much lower ($\sim 10^3 P_d$) inside the newly accreted shell. Taking a value in between, the top layer of the stellar envelope (with an initial temperature less than $T_{\max}$) is heated radiatively to a temperature $\sim T_{\max}$ on timescales of $\sim 10^5 P_d \sim 10^2$ yr. Due to the limitation of our computational resources, our models are computed for $\sim 10^3 P_d$, which is much shorter than $t_{\rm diff}$, so that the initial temperature distribution is not significantly modified (Fig. 12*b*). Convection inside the envelope may reduce the timescale by an order of magnitude. However, if the high $\dot{M}$ is sustained for a duration of $\sim t_{\rm diff}$, the temperature minimum near the original stellar surface would vanish. The ionization of this region and the reduction of the temperature gradient also act to suppress convection. Consequently, the size of the stellar envelope may undergo some adjustment. (See also the remarks in § 5.2 below.)

*Mass and angular momentum transfer onto the star.*—In addition to the thermal energy transport, both mass and

angular momentum are transferred to the accreting star. The incoming mass spreads rapidly over the surface, moves up to the polar axis, and forms a shell around the star. The density in the shell (at $t = 1000P_d \sim 1$ yr) reaches $\sim 5 \times 10^{-6}$ g cm$^{-3}$ at its base, but at the photosphere's surface it remains $\sim 10^{-8}$ g cm$^{-3}$. The total mass in the shell reaches $\sim 10^{-4}\ M_\odot$. The inner part of the entire domain (Fig. 16) indicates a smooth density transition from the disk to the star.

As the newly accreted matter arrives on the stellar envelope, it also induces angular momentum transport despite the fact that $\Omega$ interior to $d_{max}$ is much reduced from the local Keplerian values. The rate of angular momentum transfer due to advection ($\dot{J}_{adv}$) and that due to viscous stress ($\dot{J}_{vis}$) were illustrated in Figure 13*b*. Within the stellar envelope, the acquired angular momentum is further redistributed. If the rate of angular momentum redistribution in the stellar envelope is faster than $\dot{J}_{tot}$, $\Omega$ at the surface would remain small compared with $\Omega_K$ for the duration of $\sim M_*/\dot{M}$. However, if the internal redistribution is ineffective, the surface region would quickly spin up to the breakup velocity unless angular momentum may be lost from the star through stellar wind or magnetosphere-disk interaction (Königl 1991; Shu et al. 1994). On the basis that the circularization timescale for close binary T Tauri stars is $\ll 10^5$ yr (Mathieu 1994), we speculate that the internal redistribution of angular momentum is probably an efficient process. Thus, we approximate the efficiency of angular momentum redistribution with a viscosity prescription similar to the $\alpha$ prescription for disks, where the relevant lengthscale is now the vertical pressure scale height. Equation (8) includes this automatically. However, since this results in a strong dissipation within the envelope, which alters the thermal stratification, we reduce $\alpha$ by a factor of $10^{-3}$ in the stellar envelope. The convection present nevertheless transports angular momentum efficiently.

### 5.2. *Low-Flux Model*

To study the low mass-infall case, we calculated the evolution of an $\dot{M} = 10^{-7}\ M_\odot$ yr$^{-1}$ model (model 3). For the viscosity we adopted $\alpha = 0.01$. These model parameter are identical to those used by Bertout & Regev (1992) in their study of T Tau and are somewhat typical for the classical T Tauri systems in general. Again, we followed the evolution of the system for over $10^3$ dynamical timescales. During the initial stages, the disk follows a similar evolutionary pattern as the standard case until reaching a quasi-stationary state. The density distribution and velocity vectors of the final state are plotted in Figure 17, and the temperature and radiative flux are plotted in Figure 18. The radiative-flux vectors are purely radial inside the star and directed vertically in the disk. Here the thin-disk approximation is well justified.

The reader may note that the radius of star has somewhat increased, to $R \sim 1.07R_*$ (cf. also model 1). The envelope is readjusting in time, primarily because the initial one-dimensional envelope structure has been constructed by including explicitly a convective flux, as common in stellar model calculations. In contrast, the two-dimensional calculations are purely radiative and do not contain explicit convection terms. However, due to convective instability, convection begins to set in with somewhat different heat-transport properties. Hence, the initial structure has adjusted slightly in the two-dimensional simulations. This effect has been verified in test calculations with no accretion at all. The disk structure reaches an asymptotic state such that the radial distribution of $\rho_c$, $T_c$, and $\Omega$ at the disk midplane no longer undergo any significant changes (Fig. 19).

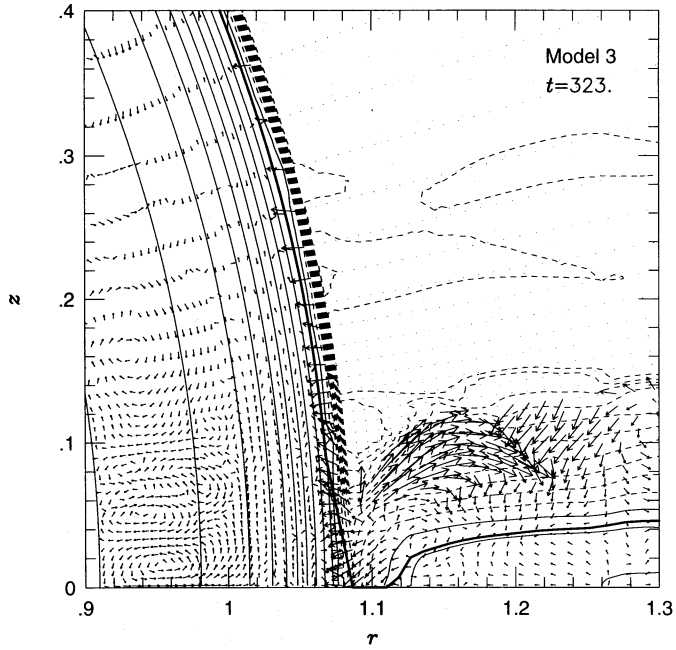


FIG. 17.—Density contours and velocity vectors in the inner regions for the final model 3.

In the steady state solution, there is a pronounced optically thin gap between the disk and the stellar surface. The radius of maximum $\Omega$ is contained in the optically thin gap (Fig. 19*c*) so that the viscous dissipation remains intense, but the transparency of the region reduces the efficiency of radiation transfer. Since the system is treated in the one-temperature approximation, the possibility of a thermal instability (corona formation) is excluded in the present

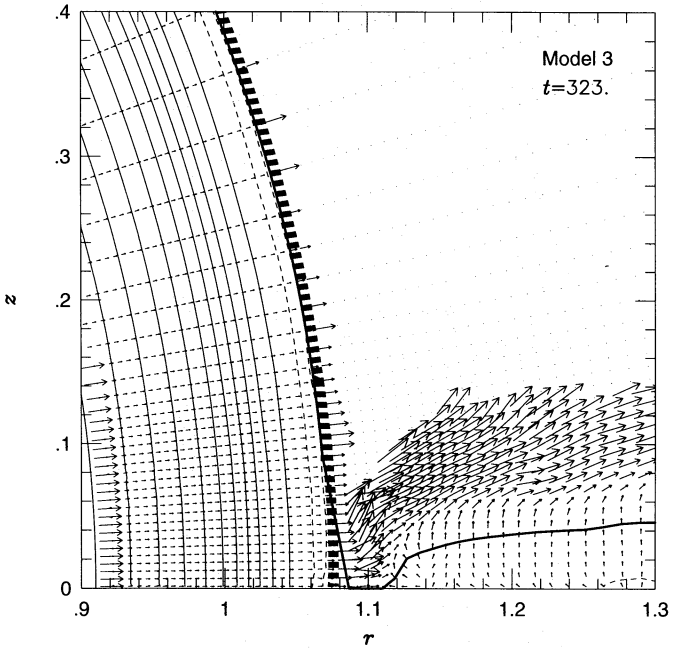


FIG. 18.—Temperature contours and radiative-flux vectors in the inner regions for the final model 3.

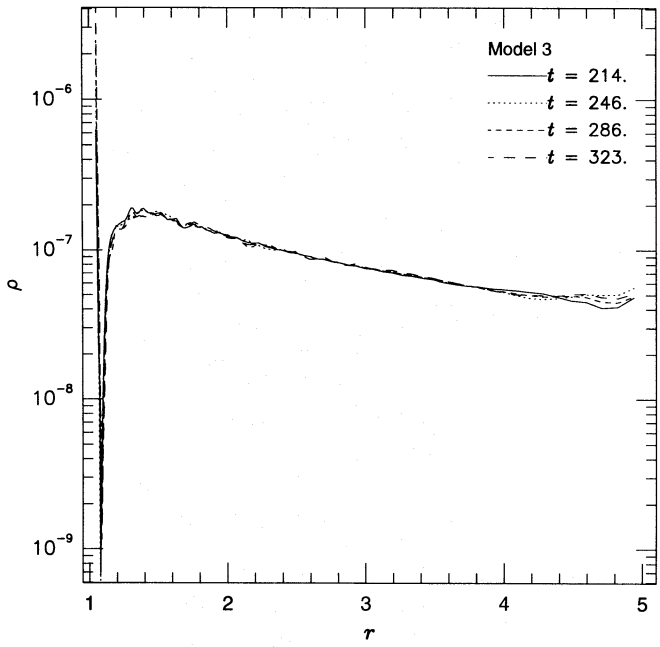


FIG. 19*a*

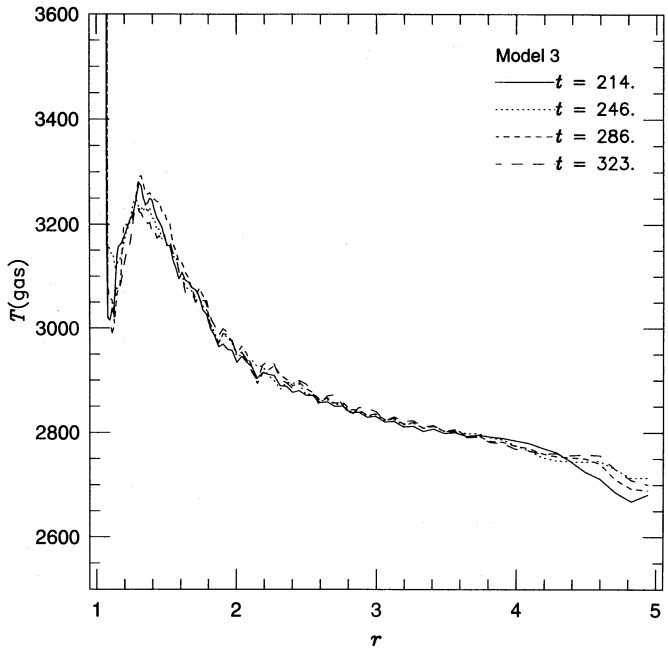


FIG. 19*b*

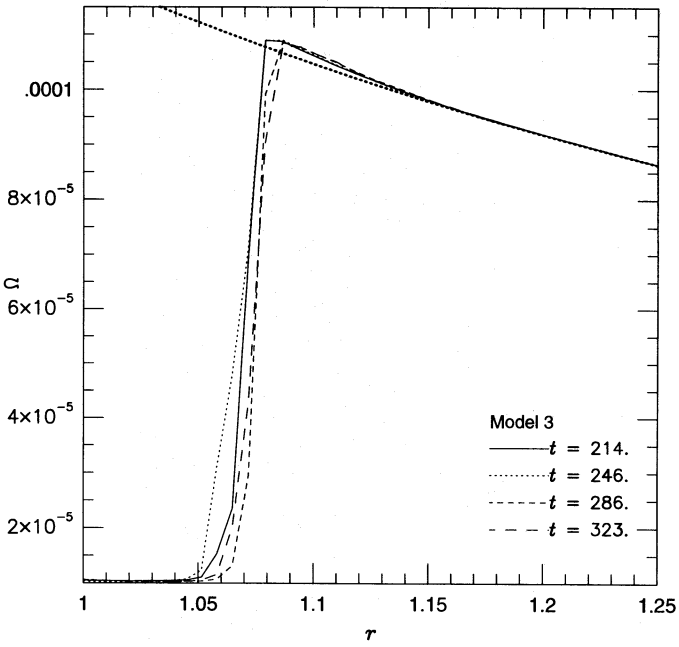


FIG. 19*c*

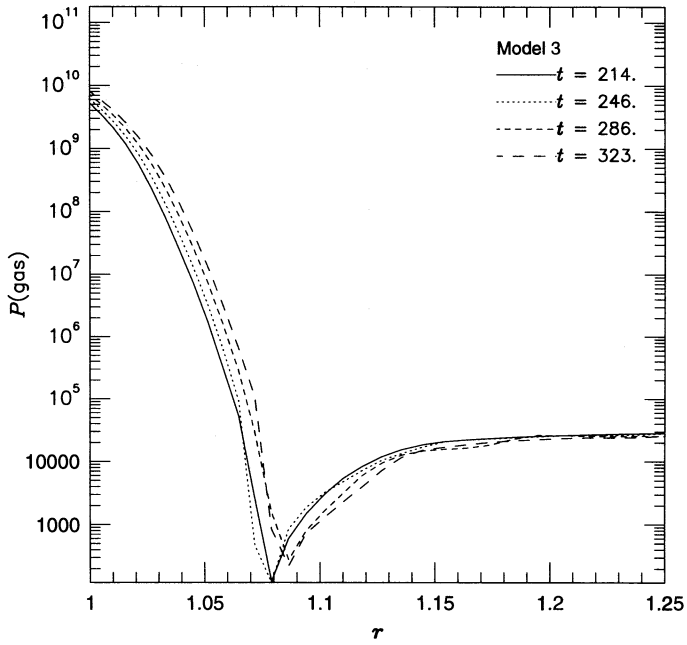


FIG. 19*d*

FIG. 19.—(*a*) Density (g cm$^{-3}$), (*b*) temperature (K), (*c*) angular velocity (s$^{-1}$), and (*d*) pressure (g cm$^{-1}$ s$^{-2}$), in the midplane of the disk, for model 3 at four different times.

computation. Although the continuum opacity may be less than unity, this gap is opaque to line radiation. Note also that in this case the angular velocity is super-Keplerian just outside its maximum (Fig. 19*c*). This is caused by the inwardly directed pressure gradient at this point (Fig. 19*d*). The radial infall velocity reaches slightly supersonic speed ($M_c \sim 1.5$) at this location, in contrast to the arguments of Popham & Narayan (1992). In this case, however, the flow is not stationary but varies in time with subsonic velocities at certain time intervals.

### 5.3. *Dependence on Viscosity*

To study directly the influences of viscosity we also performed calculations for two additional models with a constant $\nu$ of $10^{13}$ cm$^2$ s$^{-1}$ and $10^{15}$ cm$^2$ s$^{-1}$, which correspond in the vicinity of the protostar approximately to $\alpha = 0.01$ and 1.0, respectively. The mass-infall rate is identical to the standard model, i.e., $\dot{M} = 10^{-6}\ M_\odot$ yr$^{-1}$. The asymptotic quasi-equilibrium solutions for the low-viscosity model are similar to that in the standard model despite the difference

between the functional forms of the viscosity prescription. The thickness and the thermal structure of the BL are determined only by the magnitude of viscosity.

Detailed comparison between the two modified models shows that in the high-viscosity model the disk inflow soon reaches a smooth steady state, while for a low $\nu$ the flow within the disk is very oscillatory and dampens on a much longer timescale. The maximum radial infall in the high-viscosity model never exceeds a Mach number of 0.8; the other case has much smaller velocities. The radius at which a maximum value of $\Omega$ is attained occurs at $r = 1.1R_*$ in the low-viscosity model and $1.22R_*$ in the high-viscosity model (Fig. 20). The steeper gradient of the angular velocity in the high-viscosity model produces a higher dissipation rate and consequently a higher temperature in the disk/star interface. Thus, the BL disk thickness increases with $\nu$.

Since the diffusion rate is smaller in the low-viscosity case, the BL region has a relatively large surface density and optical depth. Thus, the UV excess and line emission are weaker than in the high-viscosity case. The combined measurement of line strength and the mass accretion rate may provide important information on the magnitude of viscosity.

## 6. SUMMARY

In this paper, we presented a detailed analysis of the structure of the boundary layer between a protostar and its surrounding disk. Our results indicate that the structure of the disk is sensitively determined by the mass-transfer rate.

1. In the limit of high mass-transfer rate ($\dot{M} = 10^4\ M_\odot\ \mathrm{yr}^{-1}$), such as the situation during the outburst stage in FU Orionis systems, the entire stellar surface is engulfed by the opaque disk gas. The thickness of the disk is comparable to its radius. The disk is opaque throughout the inner region. Near the stellar surface, radiation is transferred primarily in the outward radial direction by both radiative and advective processes. The midplane temperature of the inner region of the disk within a few stellar radii from the stellar surface well exceeds $10^5$ K. Due to a relatively modest effective temperature at the disk's surface, no significant UV excess is expected. In fact, there are no distinguishable features in the spectral energy distribution that may be identified as being generated in separable regions of the star-disk interface.

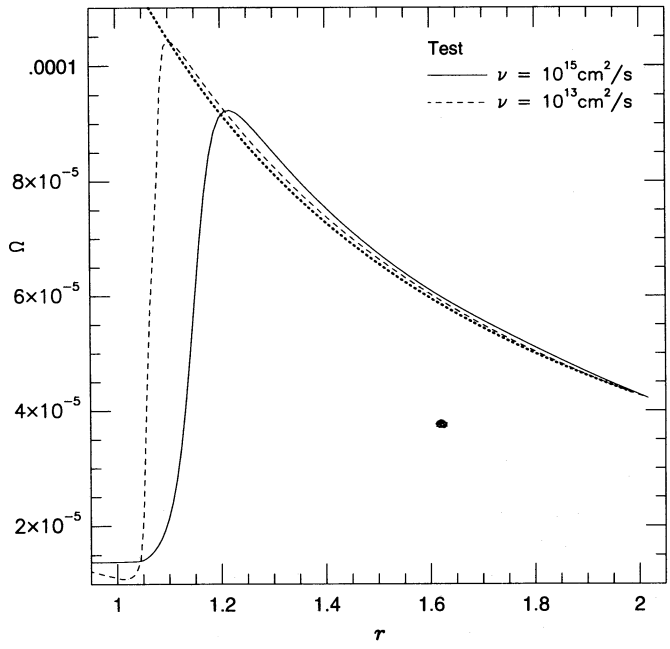


FIG. 20.—Angular velocity ($\mathrm{s}^{-1}$) in the disk midplane for two models with a constant kinematic viscosity. The dotted line indicates the Keplerian value.

Convective instability is suppressed in inner regions of the disk. Although our results indicate the persistent presence of a convective layer interior to the stellar surface, an inward flux of radiative heat reduces a temporary temperature inversion on a timescale comparable to the duration of typical FU Orionis outbursts (i.e., a few decades). If such a mass accretion rate is maintained, the stellar envelope would evolve toward a radiative state with a monotonically decreasing temperature and a slightly larger radius.

The newly accreted material arrives onto the stellar envelope at all latitudes, although the mass flux per unit area at the equator is larger than that at the poles. There is clear evidence for an equator-to-pole circulation that is effective in redistributing the newly accreted material and reducing a departure from spherical symmetry in the mass distribution. However, our numerical scheme does not have sufficient resolution to adequately place a constraint on the possibility for this circulation pattern to be fragmented into several less extended cells.

The thickness of the BL, as defined by the separation between the stellar surface and the location of maximum angular frequency, is comparable to the stellar radius. The radial velocity is a fraction of a percent of the sound speed. The newly accreted material carries with it an inward flux of angular momentum. Although the viscous stress provides an opposing, outward flux of angular momentum, the existence of an $\Omega$ maximum outside the stellar surface clearly indicates a net inward flux of angular momentum. Consequently, the rotation of the stellar envelope is expected to significantly increase on a timescale shorter than the age of the central star. Many T Tauri stars are observed to be slow rotators despite the presence of circumstellar disks and evidence of active disk accretion. A possible resolution to this paradox is the presence of a stellar magnetic field. The magnetosphere-disk interaction may effectively remove excess angular momentum until the star corotates with the Keplerian frequency at the radius of the magnetosphere where the magnetic stress is balanced by the viscous stress (Königl 1991; Shu et al. 1994). In the high infall-flux case, the radius of the magnetosphere would be crashed to the stellar surface unless the field strength exceeded $\sim 1$ kG at the stellar surface. The requirement for the magnetosphere to be extended beyond the radius of maximum angular frequency is $\sim 10$ kG. Unless the field strength at the stellar surface reaches this value, angular momentum would be accreted with mass, and rotation of the stellar envelope would increase.

2. For the mass-transfer rate ($10^{-7}\ M_\odot\ \mathrm{yr}^{-1}$) that is appropriate for typical T Tauri stars, the disk thickness is 1/10 the radius. In this limit, some (but not all) structural properties are adequately described by the thin-disk approximation. An optically thin gap is formed in the BL. The width of this region may be extended over a fraction of a stellar radius to larger width in the limit of lower mass-transfer rate. Although this region is tenuous, thermal instability induces it to have a much larger temperature than the

opaque surrounding regions of the disk. This thermal structure leads to the production of UV excess, optical veiling, and emission lines (Bertout et al. 1988; Hartigan et al. 1991). An inner hole has been observed in several protostellar disks (Edwards et al. 1993). One possible interpretation is that it indicates the existence of a magnetosphere interior to which disk flow is disrupted (Hartmann 1994). This scenario is supported by the observed luminosity variations, which have been interpreted as hot spots on the stellar surface. It is tempting to suggest that the presence of optically thin BL may provide an alternative scenario, in which case very low accretion rates are needed to account for the wide gaps. It is conceivable that the observed variations in the light curve may be associated with the onset of thermal instability in this region. A thermal instability (corona) in this optically thin region may widen the gap even more. Further analysis is needed to provide a support for this speculation.

In model 3, $\Omega$ has a maximum value in the optically thin region. A net flux of angular momentum is being transferred inward onto the star. However, mixing is efficient over a large region of the stellar envelope because it has a convective structure. Provided the stellar interior is slowly rotating initially, it is possible to retain a slow spin rate at the stellar surface despite the continuous deposition of angular momentum there.

If the emission lines are indeed produced in the optically thin gap, they would have a distinctive profile since the Doppler broadening varies rapidly with radius. In addition, unless the spin axis of the disk is parallel to the line of sight, only half the annulus in the disk near the stellar surface (where the rotation speed is slow) is visible to distant observers, in comparison with nearly the entire surface at larger disk radii.

Convection occurs in all the opaque regions of the disk. The radiation emitted at the disk's surface is generated locally by viscous dissipation, i.e., advective and radiative processes do not significantly contribute to the heat flux. Even in the vicinity of the stellar surface, the disk surface temperature decreases below 2000 K such that grains may condense there. Based on the extrapolation of our numerical results, we estimate that the dust condensation can also occur at the disk's midplane beyond 10 stellar radii from the central star. This transition radius demarcates the region over which planetary formation is possible.

The width of the BL region is an increasing function of viscosity. In this model, the radial velocity did reach marginally supersonic speed. The existence of an optically thin gap depends on our assumed prescription that an effective viscous stress may be preserved. It is also possible that turbulence may decay and viscosity may vanish in the optically thin limit. In the case, the disk flow may be self-regulated to maintain a marginally opaque and weakly viscous state or oscillate between the state of gap formation with matter accumulation and that of gap overrun. The latter possibility could lead to light-curve variation on short timescales. The value of the magnetic field needed to dominate the accretion flow in this case is $\sim 10^2$ G.

3. For the intermediate case ($\dot{M} = 10^{-6}\ M_\odot\ \mathrm{yr}^{-1}$), the disk is opaque throughout. The scale height is relatively small ($\sim 0.1r$). The energy radiated throughout the disk is essentially dissipated locally. Convection continues to exist both in the stellar envelope and on the disk. Gas in the accretion disk joins the stellar envelope via the equatorial region. A circulation pattern is clearly visible. A small fraction of the energy dissipated in the BL is advected by the circulation. However, most of the radiation emerges near the equatorial belt. The thermal structure near the poles of the star is not significantly affected.

We were unable to obtain a truly stationary solution for the intermediate case. In fact, for $10^{-6}\ M_\odot\ \mathrm{yr}^{-1} < \dot{M} < 10^{-4}\ M_\odot\ \mathrm{yr}^{-1}$, accretion flow in the inner region of a protostellar disk is subject to a thermal instability, and a steady state cannot be established. In this case, large-amplitude variations in $\dot{M}$ lead to outbursts in FU Orionis systems (Lin & Papaloizou 1985; Hartmann & Kenyon 1985; Bell & Lin 1994). We will present an analysis of the evolution of the disk during an outburst cycle in a subsequent paper.

We thank K. R. Bell and J. C. B. Papaloizou for useful conversation. D. N. C. L. thanks the Max-Planck-Institut für Astrophysik for hospitality. This work was supported in part by a special NASA astrophysics theory program that supports a joint Center for Star Formation Studies at NASA Ames Research Center, University of California, Berkeley and Santa Cruz, and also by NASA Origins of the Solar System Program grants NAGW-2422, NAGW-3599, and NCC 2-649 and also grant AST 93-15578 from the NSF. Support from the Alexander von Humboldt Stiftung is also gratefully acknowledged.

## REFERENCES

Adams, F. C., Lada, C. J., & Shu, F. H. 1988, ApJ, 326, 865
Balbus, S. A., & Hawley, J. F. 1991, ApJ, 376, 214
Basri, G., & Bertout, C. 1989, ApJ, 341, 340
———. 1993, in Protostars and Planets III, ed. E. H. Levy & J. I. Lunine (Tucson: Univ. Arizona Press), 543
Beckwith, S. V. W. 1994, in Theory of Accretion Disks—2, ed. W. J. Duschl, J. Frank, F. Meyer, E. Meyer-Hofmeister, & W. M. Tscharnuter (NATO ASI Ser. C, 417) (Dordrecht: Kluwer), 1
Bell, K. R., & Lin, D. N. C. 1994, ApJ, 427, 987
Bertout, C., Basri, G., & Bouvier, J. 1988, ApJ, 330, 350
Bertout, C., & Regev, O. 1992, ApJ, 399, 163
Cannizzo, J. K., & Wheeler, J. C. 1984, ApJS, 55, 367
Cohen, M., & Kuhi, L. V. 1979, ApJS, 41, 743
Edwards, S., et al. 1993, AJ, 106, 372
Faulkner, J., Lin, D. N. C., & Papaloizou, J. C. B. 1983, MNRAS, 205, 359
Hartigan, P., Kenyon, S. J., Hartmann, L., Strom, S. E., Edwards, S., Welty, A. D., & Stauffer, J. 1991, ApJ, 382, 617
Hartmann, L. 1994, in Theory of Accretion Disks—2, ed. W. J. Duschl, J. Frank, F. Meyer, E. Meyer-Hofmeister, & W. M. Tscharnuter (NATO ASI Ser. C, 417) (Dordrecht: Kluwer), 19
Hartmann, L., & Kenyon, S. J. 1985, ApJ, 299, 462
Hartmann, L., Kenyon, S. J., & Hartigan, P. 1993, in Protostars and Planets III, ed. E. H. Levy & J. I. Lunine (Tucson: Univ. Arizona Press), 497
Hawley, J. F., Smarr, L. L., & Wilson, J. R. 1984, ApJS, 55, 211
King, A. R., & Shaviv, G. 1984, Nature, 308, 519
Kippenhahn, R., & Thomas, H.-C. 1982, A&A, 114, 77
Kippenhahn, R., & Weigert, A. 1990, Stellar Structure and Evolution (Berlin: Springer)
Kley, W. 1989, A&A, 208, 98
———. 1991, A&A, 247, 95
Kley, W., Papaloizou, J. C. B., & Lin, D. N. C. 1993a, ApJ, 409, 739
———. 1993b, ApJ, 416, 679
Königl, A. 1991, ApJ, 370, L39
Lin, D. N. C., Hayashi, M., Bell, K. R., & Ohashi, N. 1994, ApJ, 435, 821
Lin, D. N. C., & Papaloizou, J. C. B. 1980, MNRAS, 191, 37
———. 1985, in Protostars and Planets II, ed. D. C. Black & M. S. Mathews (Tucson: Univ. Arizona Press), 981
Lynden-Bell, D., & Pringle, J. E. 1974, MNRAS, 168, 603
Mathieu, R. D. 1994, ARA&A, 32, 465
Murray, S., & Lin, D. N. C. 1992, ApJ, 384, 177
Narayan, R., & Popham, R. 1993, Nature, 362, 820

Narayan, R., & Popham, R. 1994 in Theory of Accretion Disks—2, ed. W. J. Duschl, J. Frank, F. Meyer, E. Meyer-Hofmeister, & W. M. Tscharnuter (NATO ASI Ser. C, 417) (Dordrecht: Kluwer), 293
Papaloizou, J. C. B., & Stanley, G. Q. G. 1986, MNRAS, 220, 593
Pringle, J. E. 1981, ARA&A, 19, 137
Popham, R., & Narayan, R. 1991, ApJ, 370, 604
———. 1992, ApJ, 394, 255
Popham, R., Narayan, R., Hartmann, L., & Kenyon, S. 1993, ApJ, 415, 127
Sargent, A. I., & Beckwith, S. V. W. 1987, ApJ, 323, 294
Sargent, A. I., Beckwith, S. V. W., Keene, J., & Masson, C. R. 1988, ApJ, 333, 936
Shakura, N. I., & Sunyaev, R. A. 1973, A&A, 24, 337
Shu, F., Najita, J., Galli, D., & Ostriker, E. 1993, in Protostars and Planets III, ed. E. H. Levy & J. I. Lunine (Tucson: Univ. Arizona Press), 3
Shu, F., Najita, J., Ostriker, E., Wilkin, F., Ruden, S., & Lizano, S. 1994, ApJ, 429, 781
Strom, K. M., Kepner, J., & Strom, S. E. 1995, ApJ, 438, 813
Tassoul, J.-L. 1978, Theory of Rotating Stars (Princeton: Princeton Univ. Press)
Tayler, R. J. 1980, MNRAS, 191, 135
Tschäpe, R., & Kley, W. 1993, A&A, 273, 169